

Structural, magnetic, magnetocaloric and magnetostrictive properties of $\text{Pb}_{1-x}\text{Sr}_x\text{MnBO}_4$ ($x = 0, 0.5, 1.0$)

Jake Head,^a Pascal Manuel,^b Fabio Orlandi,^b Minki Jeong,^a Martin R. Lees,^c Rukang Li,^{de} Colin Greaves,^{f*}

^a School of Physics and Astronomy, University of Birmingham, Birmingham B15 2TT, UK

^b ISIS Facility, STFC Rutherford Appleton Laboratory, Didcot OX11 0QX, UK

^c Department of Physics, University of Warwick, Coventry, CV4 7AL, UK

^d Beijing Centre for Crystal Research and Development, Key Laboratory of Functional Crystals and Laser Technology, Technical Institute of Physics and Chemistry, Chinese Academy of Sciences, Beijing 100190, P.R. China.

^e University of Chinese Academy of Science, Beijing 100049, P.R. China

^f School of Chemistry, University of Birmingham, Birmingham B15 2TT, UK

Abstract

The solid solution $\text{Pb}_{1-x}\text{Sr}_x\text{MnBO}_4$ is reported with an orthorhombic, $Pnma$, structure throughout; here studies on compounds with $x = 0, 0.5$ and 1 are described. The structure contains chains of MnO_6 octahedra that exhibit intra-chain ferromagnetic (FM) order at low temperatures. Neutron powder diffraction (NPD) reveals dominant FM order in PbMnBO_4 ($T_c = 30$ K), whereas SrMnBO_4 is primarily antiferromagnetic (AFM) with $T_N = 16$ K; the difference is related to the link between the chains that involves the BO_3 groups. PbMnBO_4 has its moment along a but also has a previously unreported AFM contribution along c (magnetic space group $Pnm'a'$), whereas SrMnBO_4 has its moment along a but also a FM canting along c (magnetic space group $Pn'm'a$). The end members show distinct magnetostriction at T_c/T_N which correlates with the different magnetic exchange in these compounds. NPD in variable applied magnetic field shows that SrMnBO_4 is converted to fully FM at 8 T. The behavior above the magnetic ordering temperature is consistent with short-range FM correlations within the chains, which is particularly apparent in PbMnBO_4 . The magnetocaloric effect (MCE) has been measured and compared with those previously reported for the mineral gauddefroyite. PbMnBO_4 has excellent MCE behavior, especially near T_c , 30 K. The strong FM exchange within the chains and FM correlations above T_c are vital for the MC properties.

Introduction

The magnetocaloric effect (MCE) is an important phenomenon which can result in a large temperature decrease if a magnetic field applied to a magnetic material is reduced to zero under adiabatic conditions. The effect relates directly to the positive entropy change (ΔS) that occurs when the magnetic field is removed and the moments disorder; typically, it is largest near the Curie temperature for a paramagnet-ferromagnet phase transition but is also large for paramagnetic lanthanide compounds at low temperatures. The adiabatic conditions determine that ΔS causes cooling of the material. Adiabatic magnetic cooling is highly attractive because it potentially has an energy efficiency approaching 100% of the Carnot maximum and has recently attracted much attention for ambient temperature refrigeration.¹⁻³ However there remains a significant need for MCE materials for low temperature applications, especially near 20 K for efficient liquefaction of hydrogen.⁴⁻⁷ This will become more important as hydrogen features strongly in an energy framework, and the production of liquid hydrogen will be critical for storage and transport. The most practical material is $\text{Gd}_3(\text{Ga,Fe})_5\text{O}_{12}$ (GGIG), but its MCE is still small with $\Delta S = -7.5 \text{ J kg}^{-1} \text{ K}^{-1}$ at 20 K with a field change of 5 T.⁷ Although intermetallics, e.g. RA_2 (R=rare earth) can have very good MCE properties at $\sim 20 \text{ K}$,⁸ they lack the necessary chemical stability in the presence of gaseous and liquid H_2 .⁷ There remains, therefore, a need for materials which display the required characteristics for hydrogen liquefaction: high entropy change at $\sim 20 \text{ K}$ using relatively low field changes ($\sim 2 \text{ T}$) which can be achieved without using superconducting magnets; a rapid response to the change in field. Ideally, the materials would be lanthanide-free to avoid possible issues with sustainability.

Frustrated magnetic materials were predicted to offer high potential for improved MCE properties (especially low field behavior and speed of temperature response) in accordance with theoretical considerations.^{9,10} The predicted advances were based on the highly degenerate magnetic ground states in Kagomé, garnet and pyrochlore lattices or even molecular systems. These predictions were subsequently confirmed experimentally for the pyrochlore $\text{Gd}_2\text{Ti}_2\text{O}_7$.¹¹ Some magnetically frustrated metal organic framework materials containing chains of lanthanide ions, e.g. $\text{Ln}(\text{HCOO})_3$ (Ln = lanthanide) have also shown excellent MCE properties, but their efficacy is highest below 4 K.¹²⁻¹⁵ The mineral gaudfroyite [$\text{Ca}_4\text{Mn}_3\text{O}_3(\text{BO}_3)_3(\text{CO}_3)$] is hexagonal, $P6_3/m$, with 1D

chains of edge-linked Mn^{3+}O_6 octahedra¹⁶ and the Mn ions located on a 2D Kagomé lattice perpendicular to the chains (Fig. 1(a)); it was demonstrated to have excellent low-field MCE properties: from 0–2 T, $\Delta S = -7 \text{ J kg}^{-1} \text{ K}^{-1}$ at 11 K and $\Delta S = -4 \text{ J kg}^{-1} \text{ K}^{-1}$ at 20 K.¹⁷ The structural and magnetic features considered to be important for these properties are:

- each Mn chain displays ferromagnetic (FM) coupling;
- antiferromagnetic (AFM) exchange between the chains is frustrated and results in a $q = 0$ structure with 120° between the magnetic moments below 10.2 K;¹⁸
- short-range FM order within the chains above T_N allows for good low-field MCE behavior for $T > T_N$.

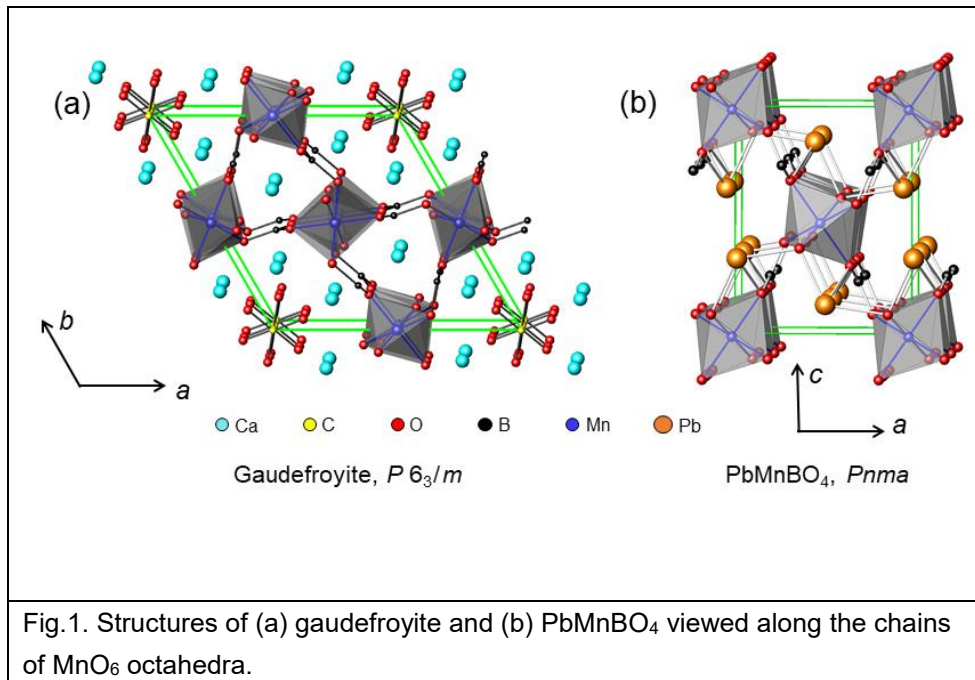


Fig. 1(a) shows that the chains of octahedra are linked by planar borate (BO_3^{3-}) groups to form channels between the chains; these are occupied by Ca^{2+} ions and disordered carbonate (CO_3^{2-}) ions. The MCE properties of gaufreyite

encouraged us to look for materials with related structural and magnetic characteristics. PbMnBO_4 was of particular interest and has an orthorhombic structure, $Pnma$, with similar chains of MnO_6 octahedra parallel to the b -axis (Fig. 1(b)), which now display both intra- and inter-chain FM order below $\sim 31 \text{ K}$.¹⁹ Although not magnetically frustrated, density functional theory calculations indicate that the intra-chain exchange constant is an order of magnitude larger than for inter-chain exchange^{20,21} In addition, there is strong experimental evidence for short-range FM order within the chains at temperatures significantly above T_c from magnetic measurements,¹⁹ specific heat measurements²² and from ferromagnetic resonance.²³

Notwithstanding the weight penalty of containing Pb, the interesting magnetic properties of PbMnBO_4 , and the absence of magnetic frustration in contrast to gauderoyite, a detailed neutron powder diffraction (NPD) study of its structural and magnetic behavior in magnetic fields has been conducted in order to provide new guidance for new materials for practical MCE behavior near 20 K. The study also resulted in the synthesis of two new compounds – SrMnBO_4 and $\text{Pb}_{0.5}\text{Sr}_{0.5}\text{MnBO}_4$ – which, although structurally related to PbMnBO_4 , display very different magnetic behavior. These differences provide a basis for the discussion of the magnetic exchange interactions in these phases, and useful experimental data for designing new MCE materials. The MCE properties of all materials were measured.

Experimental methods

The samples examined were synthesized from Sigma-Aldrich chemicals: Mn_2O_3 (99.9%), PbO (99.9%), SrCO_3 (99.9%) and $^{11}\text{B}_2\text{O}_3$ (>99% ^{11}B). The ^{11}B -enriched B_2O_3 was initially converted to H_3BO_3 by dissolving in the minimum amount of H_2O and drying overnight at 60 °C. At higher temperatures partial dehydration to HBO_2 can occur. For the synthesis of PbMnBO_4 , the problems reported previously¹⁹ were not encountered and phase pure samples were obtained from well-mixed PbO , Mn_2O_3 and H_3BO_3 by slow heating (40°C h^{-1}) to 700 °C and holding for 10 h. This process was repeated for all samples used for characterization. SrMnBO_4 was more difficult to obtain phase pure than the Pb-containing samples, presumably because of PbO acting as a flux in the latter materials. SrMnBO_4 was synthesized by heating a mixture of SrCO_3 , Mn_2O_3 and H_3BO_3 at 25°C h^{-1} to 850°C, holding for 3 h followed by 10°C h^{-1} to 950 °C and holding for 30 h. This process was repeated to obtain the highest level of purity. $\text{Pb}_{0.5}\text{Sr}_{0.5}\text{MnO}_4$ was synthesized from two heat treatments, each comprising 50°C h^{-1} to 850 °C and holding for 6 h.

Initial structure and sample purity characterization was achieved by X-ray powder diffraction (XRPD; Bruker D8 Advance, $\text{Cu-K}\alpha$ radiation in reflection mode). NPD data were collected on the instrument WISH at ISIS, Science and Technology Facility Council, Rutherford Appleton Laboratory.²⁴ This diffractometer provides high-quality data at low-Q and is therefore ideal for magnetic measurements. Four pairs of detectors were used, located at approximate 2θ values of 153°

(highest resolution, high Q), 122°, 90° and 58° (lower resolution, low Q); equal weighting was applied to all detectors used in the refinements. Data were collected at ambient temperature and temperatures down to 1.5 K (cryostat for $\text{Pb}_{0.5}\text{Sr}_{0.5}\text{MnBO}_4$, cryomagnet for PbMnBO_4 and SrMnBO_4); the cryomagnet produced data for SrMnBO_4 and PbMnBO_4 in applied fields up to 8 T. $\text{Pb}_{0.5}\text{Sr}_{0.5}\text{MnBO}_4$ was in powdered form (~ 2 g in a 6 mm diameter V can) whereas PbMnBO_4 (4.8 g) and SrMnBO_4 (4.2 g) were converted into discs (7 mm diameter, ~ 5 mm thick) which were sintered at the final synthesis temperature, to prevent sample movement in high fields, and loaded into 8 mm cans. Calculations of μ_r/r indicated that absorption corrections were unnecessary because of the use of ^{11}B . Structure refinements based on the NPD datasets were achieved using the GSAS-II software package.²⁵

Magnetic susceptibility measurements were obtained from a Quantum Design MPMS magnetometer. Zero field-cooled (ZFC) and field-cooled (FC) data were obtained on warming after cooling the samples in zero field and the measuring field (10 mT), respectively. The magnetic entropy change ΔS at a given field and temperature was determined indirectly²⁶ from one of the Maxwell thermodynamic relations using magnetization versus magnetic field data collected in an Oxford Instruments vibrating sample magnetometer.

Results and Discussion

Nuclear structures at ambient temperature and 1.5 K

The chains of MnO_6 octahedra in PbMnBO_4 are linked by B atoms (within BO_3 groups) and also Pb^{2+} ions (Fig. 1(b)). The Pb^{2+} ions are bonded to four O^{2-} ions on one side and have a stereochemically active lone pair of electrons opposite. It is therefore somewhat surprising to discover that Sr^{2+} can substitute for Pb^{2+} to form SrMnBO_4 and $\text{Pb}_{0.5}\text{Sr}_{0.5}\text{MnBO}_4$ (and, presumably, all compositions in the solid solution $\text{Pb}_{1-x}\text{Sr}_x\text{MnBO}_4$). However, since Pb^{2+} and Sr^{2+} have almost identical ionic radii²⁷ and bond valence sums (BVS),²⁸ if adequate space for the lone pair is available, such a substitution is plausible, but the loss of the lone pair of electrons in SrMnBO_4 would inevitably result in a significant contraction in the unit cell. It is therefore important initially to consider the structural changes that occur when Pb^{2+} is replaced by Sr^{2+} .

Table 1 Structural parameters for PbMnBO₄ at 300 K (top line) and 1.5 K (bottom line).

Atom	Site	T/K	<i>x/a</i>	<i>y/b</i>	<i>z/c</i>	100× <i>U</i> _{iso} / Å ²
Pb	4 <i>c</i>	300	0.0335(5)	0.25	0.3526(3)	1.14(6)
		1.5	0.0382(2)		0.3515(2)	0.51(6)
Mn	4 <i>a</i>	300	0	0	0	2.0(2)
		1.5				0.9(1)
O1	4 <i>c</i>	300	0.1088(7)	0.75	0.8952(5)	1.1(1)
		1.5	0.1081(3)		0.8957(3)	1.4(1)
O2	8 <i>d</i>	300	0.1687(5)	0.9544(3)	0.1881(3)	1.16(7)
		1.5	0.1666(3)	0.9532(3)	0.1891(2)	0.71(6)
O3	4 <i>c</i>	300	0.7884(7)	0.75	0.0928(4)	1.5(1)
		1.5	0.7874(3)		0.0923(3)	0.70(8)
B	4 <i>c</i>	300	0.7927(6)	0.25	0.7380(4)	1.32(9)
		1.5	0.7919(3)		0.7377(3)	0.57(8)

Space Group *Pnma*;. 300 K: $a = 6.69380(5) \text{ \AA}$; $b = 5.94182(4) \text{ \AA}$; $c = 8.63691(7) \text{ \AA}$
1.5 K: $a = 6.7078(1) \text{ \AA}$; $b = 5.93651(7) \text{ \AA}$; $c = 8.6063(1) \text{ \AA}$
Magnetic moment (*Pnm'a'*) at 1.5 K: $\mu_x = 3.42(4) \mu_B$; $\mu_y = 0 \mu_B$; $\mu_z = 0.41(6) \mu_B$; $\mu_{total} = 3.44(4) \mu_B$
Overall wR_p : 0.052 (153° + 122° detectors, 300 K); 0.078 (122° + 90° detectors, 1.5 K).

NPD data were collected at 300 K and 1.5 K from all three compounds. The synthesis of pure samples of SrMnBO₄ had proven difficult, but the final sample used appeared pure from an XRPD refinement. However, two contaminants were detected in the NPD patterns: SrB₂O₄ (4 wt%) and Mn₂O₃ (3 wt%). These well-characterized impurities were therefore included as additional phases and caused no problems in the refinement; the other samples were phase pure. The refinements were straightforward without any constraints and allowed independent isotropic displacement parameters (IDPs) to be varied. Refinement suggested all sites to be fully occupied and they were therefore fixed at unity. The *Pnma* space group of PbMnBO₄ is retained in all samples, but there are major changes to the unit cell dimensions on substitution, as indicated by the refined structural parameters in Tables 1-3. The tables reveal only minor structural changes on cooling to 1.5 K. At 300 K, the unit cell volume of SrMnBO₄ (329.728(3) Å³) is 4% smaller than that of PbMnBO₄ (343.519(5) Å³), consistent with the loss of the lone pair of electrons. It is important to note, however, that the full substitution of Sr causes little change in *b* (0.6% increase in the direction of the MnO₆ chains) but a large decrease in *a* (8%) and a substantial *increase* in *c* (4%). The major

structural changes might therefore be expected to have a minor effect on magnetic exchange within the chains but are likely to influence the inter-chain properties significantly. The unit cell parameters for $\text{Pb}_{0.5}\text{Sr}_{0.5}\text{MnBO}_4$ are intermediate between those of the end members but are closer to those of SrMnBO_4 .

Table 2 Structural parameters for $\text{Pb}_{0.5}\text{Sr}_{0.5}\text{MnBO}_4$ at 300 K (top line) and 1.5 K (bottom line).

Atom	Site	T/K	x/a	y/b	z/c	$100 \times U_{iso} / \text{Å}^2$
Pb/Sr ^a	4c	300	0.0017(3)	0.25	0.3532(4)	2.2(1)
		1.5	-0.0007(3)		0.3526(2)	0.80(7)
Mn	4a	300	0	0	0	0.4(2)
		1.5				0.9(1)
O1	4c	300	0.111(1)	0.75	0.8996(5)	1.1(1)
		1.5	0.1190(3)		0.9032(3)	1.02(9)
O2	8d	300	0.1652(8)	0.9551(4)	0.1822(2)	2.3(1)
		1.5	0.1771(3)	0.9526(2)	0.1826(2)	1.11(6)
O3	4c	300	0.749(1)	0.75	0.0964(5)	3.7(2)
		1.5	0.7583(3)		0.0929(3)	1.03(9)
B	4c	300	0.8026(7)	0.25	0.7440(4)	0.6(1)
		1.5	0.7987(3)		0.7433(3)	0.75(7)

^a The Pb/Sr site occupancy was constrained to 0.5/0.5 since refinement resulted in no change.

Space Group *Pnma*;. 300 K: $a = 6.31306(9) \text{ Å}$; $b = 5.97078(6) \text{ Å}$; $c = 8.87951(9) \text{ Å}$
1.5 K: $a = 6.2989(1) \text{ Å}$; $b = 5.96542(7) \text{ Å}$; $c = 8.8742(1) \text{ Å}$

Magnetic moment (*Pn'm'a*) at 1.5 K: $\mu_x = 3.71(1) \mu_B$; $\mu_y = 0 \mu_B$; $\mu_z = 0.0 \mu_B$; $\mu_{total} = 3.71(1) \mu_B$

Overall wR_p : 0.063 (153° + 122° detectors, 300 K); 0.064 (122° + 58° detectors, 1.5 K).

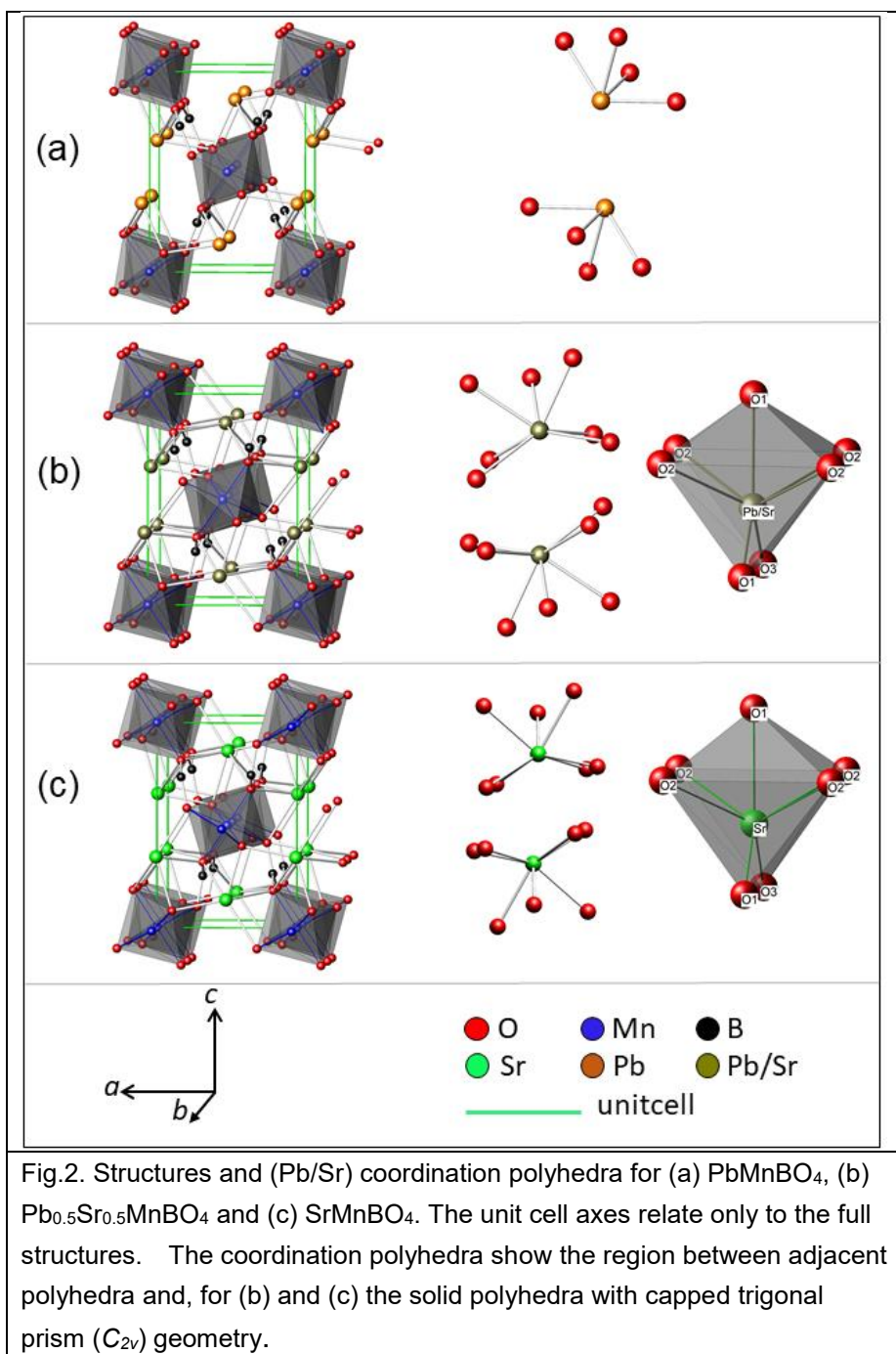
Table 4 and Fig. 2 provide detailed information to allow analysis of the structural differences between the three synthesized compounds. Table 4 provides bond distance and angle data relating to the MnO_6 chains (important for intra-chain magnetic interactions) and the Pb/Sr coordination; it also provides BVS information for these ions. Some data from the related mineral, gaudefroyite, are also included. For all four compounds we see that the MnO_6 octahedra show large Jahn-Teller distortions with the longest and shortest Mn–O bonds (to O3 and O1, respectively) being to the two O atoms in the linking edge. This will be considered later with respect to the

Table 3 Structural parameters for SrMnBO_4 at 300 K (top line) and 1.5 K (bottom line).

Atom	Site	T/K	x/a	y/b	z/c	100×U _{iso} / Å ²
Sr	4c	300	-0.0119(3)	0.25	0.3555(2)	0.57(6)
		1.5	-0.0136(3)		0.3548(2)	0.50(8)
Mn	4a	300	0	0	0	0.9(1)
		1.5				0.8(1)
O1	4c	300	0.1164(5)	0.75	0.9092(3)	0.72(8)
		1.5	0.1254(3)		0.9102(3)	1.40(9)
O2	8d	300	0.1727(4)	0.9540(3)	0.1802(2)	0.99(5)
		1.5	0.1754(3)	0.9511(2)	0.1826(2)	1.28(6)
O3	4c	300	0.7320(5)	0.75	0.0940(3)	0.92(7)
		1.5	0.7334(3)		0.0907(3)	0.97(8)
B	4c	300	0.8104(4)	0.25	0.7435(3)	1.05(6)
		1.5	0.8065(3)		0.7441(3)	0.33(6)

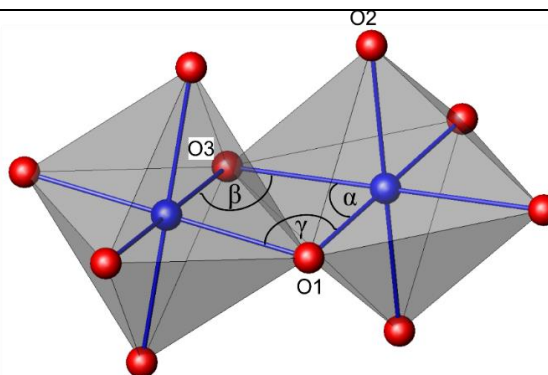
Space Group *Pnma*;
300 K: $a = 6.14892(3) \text{ \AA}$; $b = 5.97768(4) \text{ \AA}$; $c = 8.97067(6) \text{ \AA}$
1.5 K: $a = 6.12975(5) \text{ \AA}$; $b = 5.97004(6) \text{ \AA}$; $c = 8.9545(1) \text{ \AA}$
Magnetic moment (*Pn'm'a*) at 1.5 K: $\mu_x = 3.42(4) \mu_B$; $\mu_y = 0 \mu_B$; $\mu_z = 0.0 \mu_B$; $\mu_{total} = 3.42(4) \mu_B$
Overall wR_p : 0.040 (153° + 122° detectors, 300 K); 0.059 (122° + 58° detectors, 1.5 K).

intra-chain magnetic exchange. In PbMnO_4 , Pb has four bonds to O, giving the common geometry with all O atoms on one side and consistent with the lone pair of electrons situated on the opposite side. Table 4 includes a 5th O which is significantly more distant from Pb but is included for the BVS calculation. Fig. 2 shows that the lone pairs will be located in the space between adjacent Pb atoms. It is interesting that the coordination around the Pb/Sr cations in the other two compounds is quite similar with a coordination number of seven. Fig. 2 shows that the O atoms are in a single-capped trigonal prism arrangement with the cap on a rectangular face of the prism (four O2 atoms). The changes in *a* and *c* unit cell distances relate to the preferred coordination of Pb^{2+} and Sr^{2+} ions. Fig. 2 shows that in SrMnBO_4 , the Sr ions move to a more central position between the MnO_6 chains and, by attracting the chains towards it along *a*, can bond to seven O atoms in three different chains to achieve a more regular coordination than that of Pb in PbMnBO_4 . Comparison of Tables 1 and 3 shows large shifts along *a* for Sr (compared with Pb) and O3 to which Sr becomes bonded. The higher coordination number results in longer bonds which cause an expansion in the *c* direction. The similar geometry for the M^{2+} cations in both SrMnBO_4 and $\text{Pb}_{0.5}\text{Sr}_{0.5}\text{MnBO}_4$ shows



that the coordination is acceptable for both cations and Figs. 2(b) and 2(c) show that pairs of $(\text{Pb/Sr})\text{O}_7$ polyhedra exist with space between them to accommodate the Pb lone pair electrons. This coordination appears to be rare for Pb^{2+} , although a similar PbO_7 polyhedron is found in $\text{Pb}_2\text{V}_3\text{O}_9$.²⁹ Tables 1-3 show that the Pb/Sr and O IDP values for $\text{Pb}_{0.5}\text{Sr}_{0.5}\text{MnBO}_4$ are generally larger than the end-member phases, which suggests slightly different atom positions in SrO_7 and PbO_7 polyhedra, but the differences are small and consistent with the almost identical BVS

Table 4. Selected bond distances (Å) and angles (°) for PbMnO₄, SrMnBO₄, Pb_{0.5}Sr_{0.5}MnBO₄ and gaudefroyite at 300 K.



	PbMnBO ₄	SrMnBO ₄	Pb _{0.5} Sr _{0.5} MnBO ₄	Gaudefroyite ^a
Mn–O2	1.985(2) [×2]	1.953(2) [×2]	1.943(3) [×2]	1.972(1)
Mn–O1	1.881(1) [×2]	1.846(2) [×2]	1.875(3) [×2]	1.870(1)
Mn–O3	2.212(2) [×2]	2.379(2) [×2]	2.338(6) [×2]	2.235(1)
α	83.8(1)	85.21(8)	85.4(2)	85.19(5)
β	84.8(2)	77.82(9)	79.4(2)	82.45(5)
γ	103.9(2)	108.1(2)	105.5(3)	103.90(7)
Pb–O1	2.423(6) 2.342(5)	–	2.479(6) 2.355(6)	–
Pb–O2	2.434(3) [×2]	–	2.545(4) [×2] 2.777(5) [×2]	–
Pb–O3	2.991(5)	–	2.678(7)	–
Sr–O1	–	2.479(3) 2.460(3)	2.479(6) 2.355(6)	–
Sr–O2	–	2.625(2) [×2] 2.645(3) [×2]	2.545(4) [×2] 2.777(5) [×2]	–
Sr–O3	–	2.531(3)	2.678(7)	–
Mn BVS	3.12	3.15	3.10	3.17
Pb BVS	1.90		2.06	
Sr BVS		2.09	2.09	

^a Derived from Hoffmann *et al.*¹⁶

parameter for the two cations.²⁸ Table 4 shows BVS values for Mn³⁺, Pb²⁺ and Sr²⁺ which are close to their predicted values. The refinement plots for SrMnBO₄ at 300 K (122° detectors shown since their Q-range includes all low-Q peaks) are shown in Fig. 3 and those for PbMnBO₄ and Pb_{0.5}Sr_{0.5}MnBO₄ in Supplementary Information Figs. S1 and S2, respectively.

Given the significant structural differences between PbMnBO₄ and the Sr-containing phases, their magnetic properties were investigated by magnetometry and variable temperature NPD.

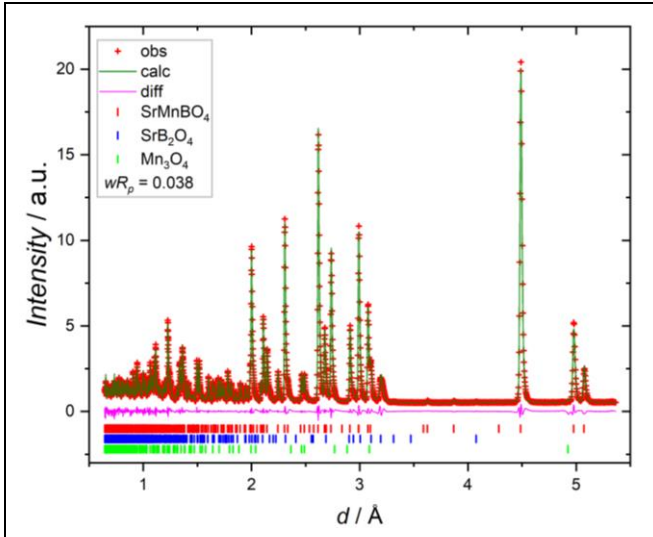


Fig. 3. Rietveld refinement plots (122° detectors) for SrMnBO₄ at 300 K.

Magnetic ordering: magnetization and NPD measurements

Plots of magnetic susceptibility (χ) and inverse susceptibility against temperature are shown in Fig. 4 for the three samples.

Qualitatively, the plots are similar and indicate a transition on cooling to a state which is either FM or has a FM component, e.g. canted AFM.

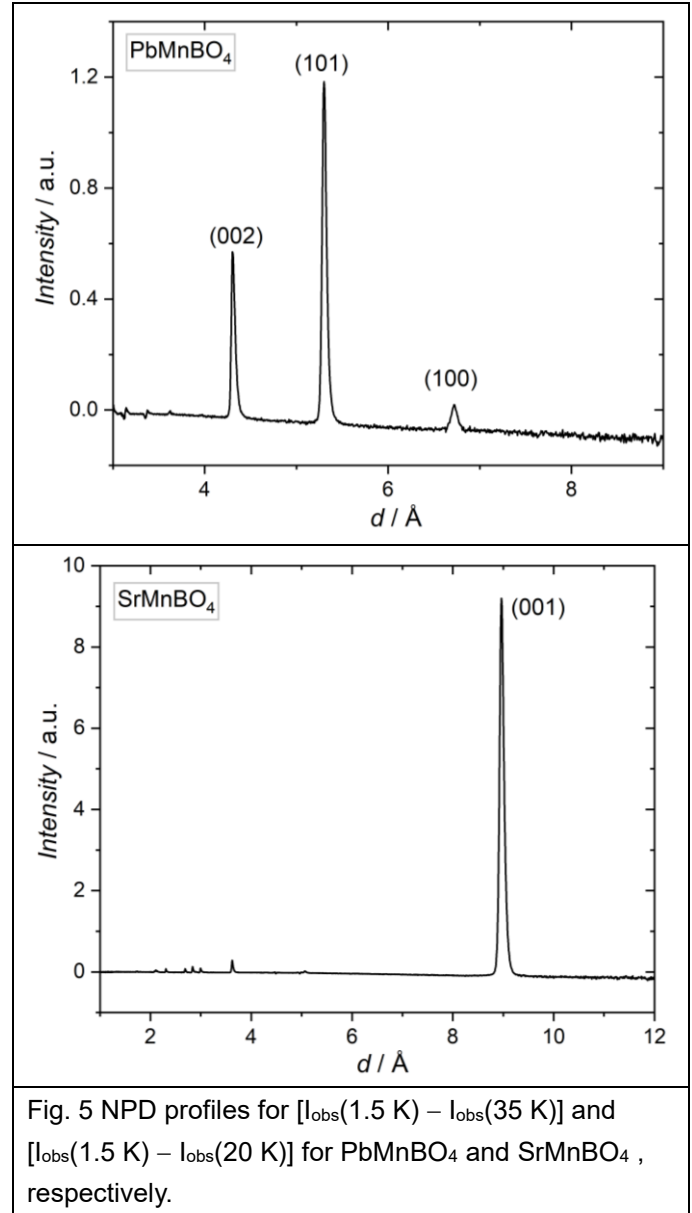
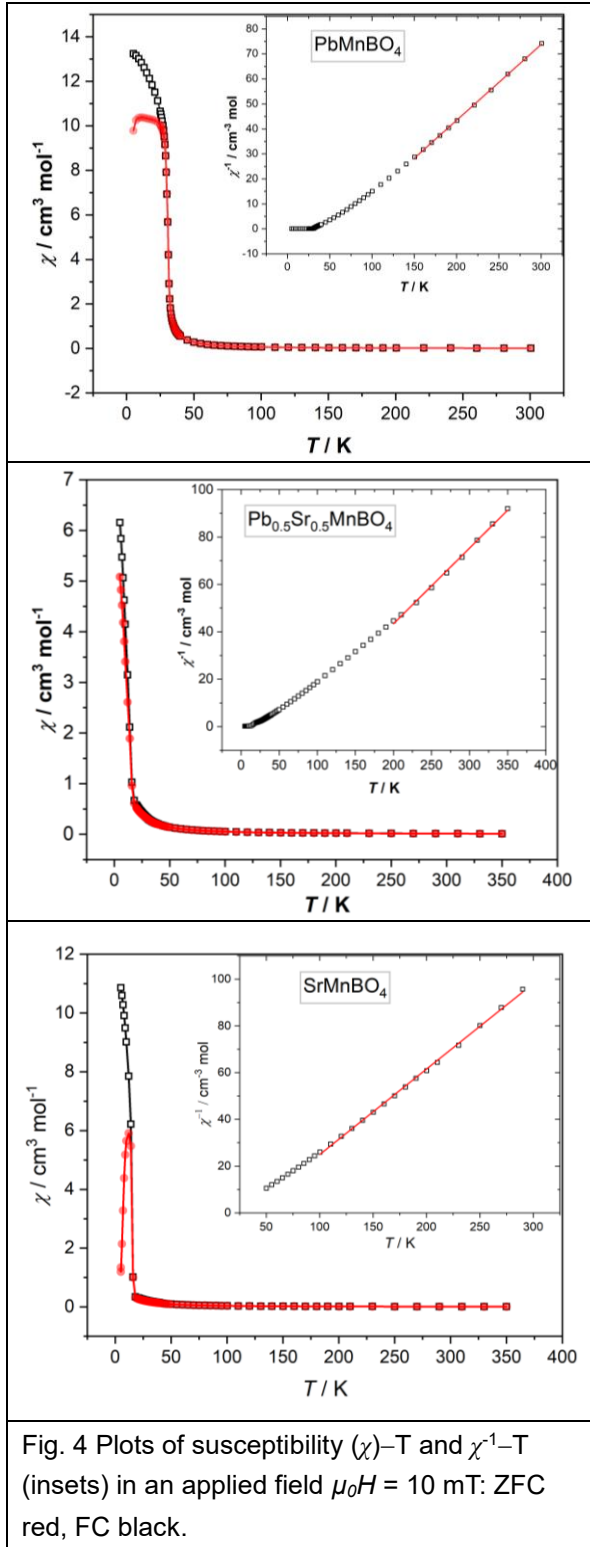
The $\chi^{-1} - T$ plots show deviations from Curie-Weiss (C-W) behavior below 150 K (PbMnBO₄), 200 K (Pb_{0.5}Sr_{0.5}MnBO₄) and 100 K (SrMnBO₄).

Analysis of the data in the C-W regions is summarized in Table 5 with estimates of the transition temperatures (corresponding to initial major deviations in the $\chi^{-1} - T$ plots) and C-W temperatures (θ).

Table 5. Magnetic parameters from susceptibility measurements.

	Ordering temperature	Curie constant (C)	μ_{eff} / μ_B	C-W temperature θ / K	Temp range / K
PbMnBO ₄	$T_c = 30.0$ K	3.30	5.1(1)	57(1)	150-300
SrMnBO ₄	$T_N = 16.1$ K	2.73	4.7(1)	32(2)	100-300
Pb _{0.5} Sr _{0.5} MnBO ₄	$T_N = 16.0$ K	3.13	5.0(1)	64(2)	200-350

The data for PbMnBO₄ are in agreement with those reported previously.¹⁹ It is seen that θ is positive for all compounds and indicates predominantly FM interactions in the C-W region. Impurities are unlikely to be responsible since Pb_{0.5}Sr_{0.5}MnBO₄ is phase pure. As was suggested for PbMnBO₄,¹⁹ the deviations from the C-W law at lower temperatures are consistent with the occurrence of short-range FM correlations, presumably within the MnO₆ chains. The effective magnetic moments, μ_{eff} , are close to the spin-only value of 4.9 μ_B , and the lack of an orbital contribution is expected for the distorted octahedral environment for Mn³⁺ ions.



The nature of the magnetically ordered state was determined from the NPD data at 1.5 K. The magnetic scattering for PbMnBO_4 and SrMnBO_4 were initially compared by subtracting the observed profiles above the transition temperature (35 K for PbMnBO_4 , 20 K for SrMnBO_4) from those at 1.5 K. The results

are shown in Fig. 5. The main magnetic peaks for PbMnBO_4 , (101) and (002), are as previously reported¹⁹ and correspond with FM order both within the chains and between the chains with the moment directed along [100]; the magnetic space group is directly related to the nuclear space

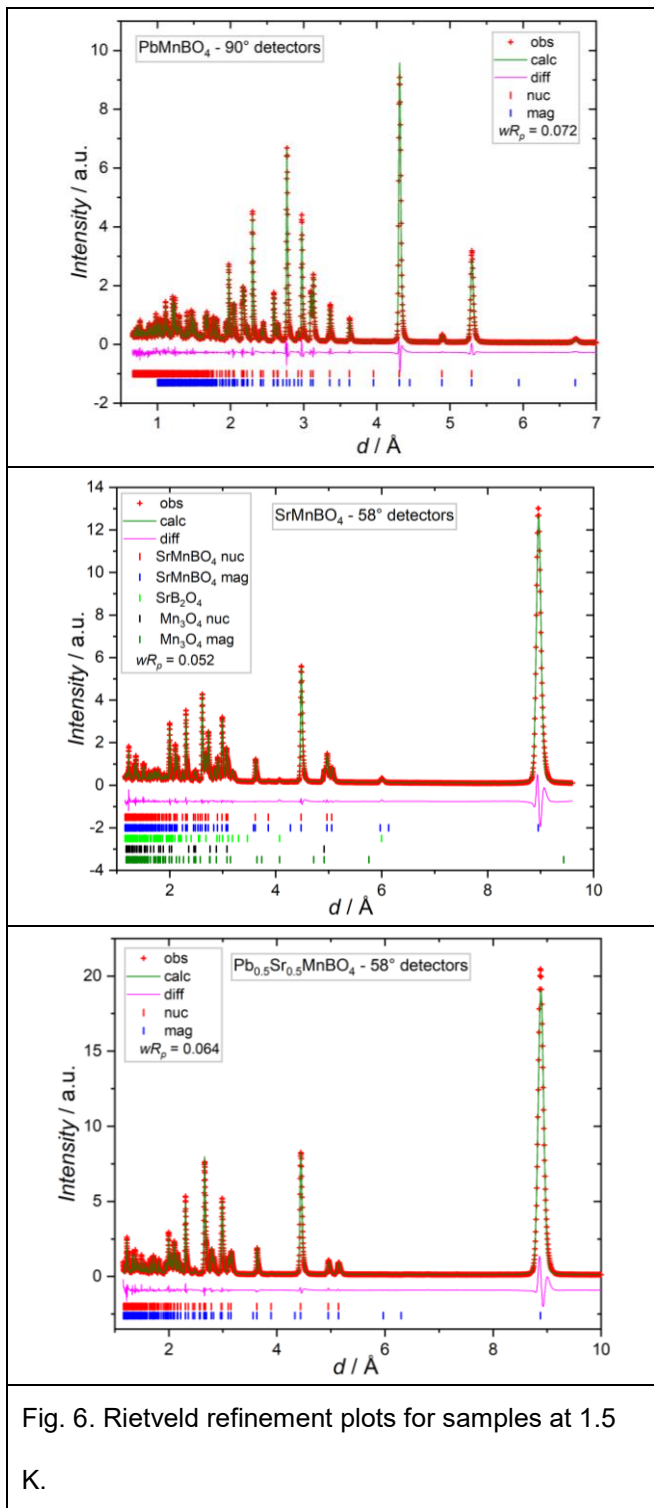


Fig. 6. Rietveld refinement plots for samples at 1.5 K.

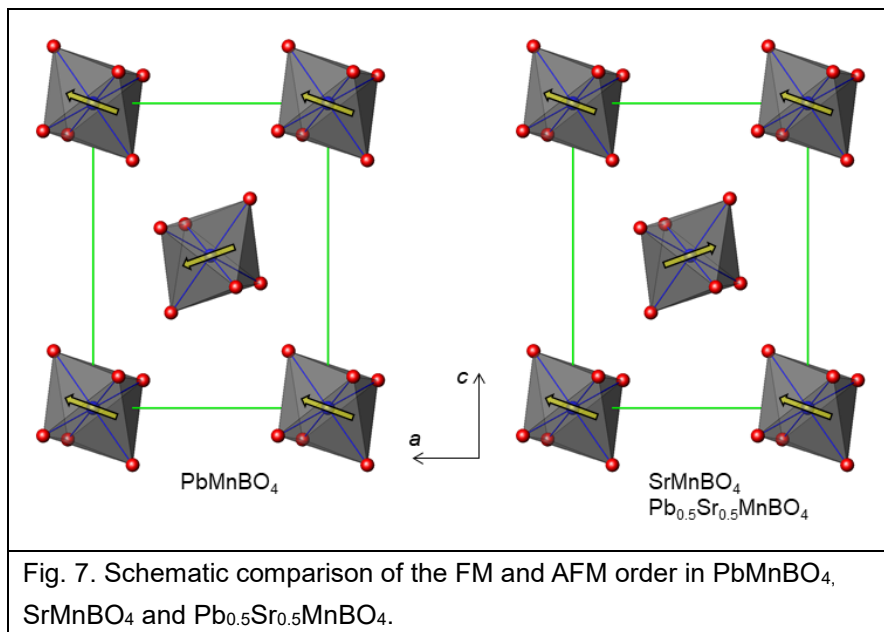
group and is $Pnm'a'$. However, Fig. 5 clearly shows a (100) magnetic peak which has not previously been reported. Although forbidden for nuclear scattering by the a -glide plane, the reflection is allowed for the a' magnetic symmetry element. The observation of (100) allows retention of the propagation vector $k = (0,0,0)$ and suggests an AFM modulation along c (perpendicular to the FM moment) which provides in-phase scattering for (100) and is consistent with $Pnm'a'$ ($m\Gamma_3+$ irreducible representation³⁰). No magnetic component along [010] was observed.

For $SrMnBO_4$, the only dominant feature is the strong (001) reflection, which is also forbidden in $Pnma$ and suggests an inter-chain AFM arrangement of the FM chains with the moment within the ab plane. The only symmetry-allowed solution is for the moment to be aligned along [100] in $Pn'm'a'$ ($m\Gamma_2+$ irreducible representation³⁰). Given that the magnetization measurements indicate a FM component to the ordered state, it is relevant to note that $Pn'm'a'$ allows canting to provide a FM moment only along [001]. $Pb_{0.5}Sr_{0.5}MnBO_4$

shows very similar magnetic features in its NPD pattern to $SrMnBO_4$ and the FM components to their susceptibilities (Fig.4) relate to this canting. The low temperature divergence between FC and ZFC

data reflects different field dependencies for the FM component of SrMnBO_4 and $\text{Pb}_{0.5}\text{Sr}_{0.5}\text{MnBO}_4$, which is also apparent in the isothermal field sweep magnetization data (*vide infra*).

The magnetic models allowed straightforward NPD refinements of the basic magnetic structures and inclusion of the small AFM moment along [001] in PbMnBO_4 was also stable to give $\mu_z = 0.41(6) \mu_B$. The FM canting moments for the Sr-containing phases were too small to provide a significant effect and μ_z was constrained to zero. The final magnetic moments are $\mu_x = 3.42(4) \mu_B$, $\mu_y = 0 \mu_B$, $\mu_z = 0.41(6) \mu_B$, $\mu_{total} = 3.44(4) \mu_B$ for PbMnBO_4 ; $\mu_x = 3.71(1) \mu_B$, $\mu_y = 0 \mu_B$, $\mu_z = 0.0 \mu_B$, $\mu_{total} = 3.71(1) \mu_B$ for $\text{Pb}_{0.5}\text{Sr}_{0.5}\text{MnBO}_4$ and $\mu_x = 3.42(4) \mu_B$, $\mu_y = 0 \mu_B$, $\mu_z = 0.0 \mu_B$, $\mu_{total} = 3.42(4) \mu_B$ for SrMnBO_4 ; these data are also provided in Tables 1-3. The moments are $\sim 10\%$ below the expected $4.0 \mu_B$ which can be attributed primarily to covalence. Fig. 6 shows Rietveld refinement plots for all samples against data for detectors which include all the lowest-Q magnetic reflections. Fig. 7 gives a schematic representation (the deviation of the moments from the *a*-axis are exaggerated) of the two magnetic arrangements viewed along [010], the direction of the MnO_6 chains. In both, the moments are purely FM within each chain.



The variation of magnetic scattering between 1.5 K and the magnetic ordering temperatures were determined by the changes in magnetic peak intensities – the (001) purely magnetic peak for SrMnBO_4 and $\text{Pb}_{0.5}\text{Sr}_{0.5}\text{MnBO}_4$ and (101) for PbMnBO_4 . The latter peak was corrected for the small

amount of nuclear intensity. Fig. 8 focuses on the variation of peak intensities with temperature near to the ordering temperature (here represented by T_c), where good compliance is expected with the

mean field scaling equation $I \propto (1 - \frac{T}{T_c})^{2\beta}$. The fitted parameters, β and T_c , are given in the inset to Fig. 8; the ordering temperatures are in reasonable agreement with the data from magnetization measurements (Table 5) but are more precise. Although the experimental data are limited, the values of β for PbMnBO_4 (0.21(1)), SrMnBO_4 (0.21(1)) and $\text{Pb}_{0.5}\text{Sr}_{0.5}\text{MnBO}_4$ (0.23(1)) are very similar and consistent with that reported for gaufreyite (0.20(2))¹⁸; they are typical of low dimensional magnetically ordered materials.^{31,32}

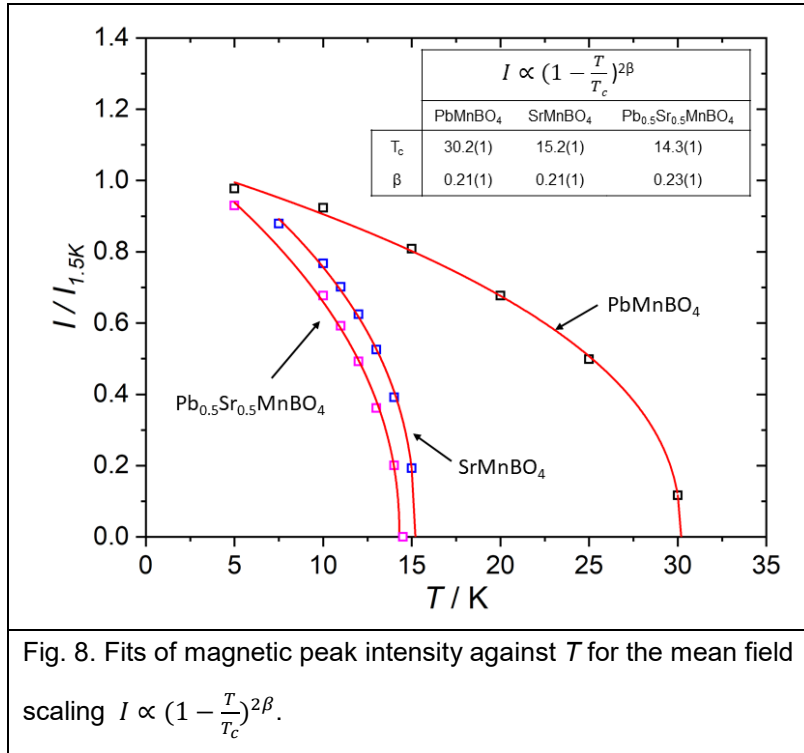


Fig. 8. Fits of magnetic peak intensity against T for the mean field scaling $I \propto (1 - \frac{T}{T_c})^{2\beta}$.

To explore the canting of the moments in the AFM Sr-containing phases, isothermal field sweep magnetization measurements were performed at 10 K and the results for all three samples are shown in Fig. 9. PbMnBO_4 shows simple FM behavior with a small coercivity of ~ 35 mT whereas SrMnBO_4 and $\text{Pb}_{0.5}\text{Sr}_{0.5}\text{MnBO}_4$ show a FM hysteresis loop at low field followed by a gradually increasing moment at higher fields. The FM component

confirms a canted AFM ground state; the form of the hysteresis loops and remanent magnetization values suggest canting moments of $0.21 \mu_B$ for SrMnBO_4 and $0.07 \mu_B$ for $\text{Pb}_{0.5}\text{Sr}_{0.5}\text{MnBO}_4$ along [001]. Such small FM components would be very difficult to detect in our NPD experiments.

Magnetostriction and magnetic exchange interactions

Careful monitoring of the unit cell dimensions during heating and cooling revealed significant changes for PbMnBO_4 and SrMnBO_4 at their magnetic phase transitions as shown in Fig. 10. No clear evidence for this spontaneous magnetostriction was found for $\text{Pb}_{0.5}\text{Sr}_{0.5}\text{MnBO}_4$. The changes observed are larger for PbMnBO_4 (FM inter-chain exchange) than SrMnBO_4 (AFM inter-chain

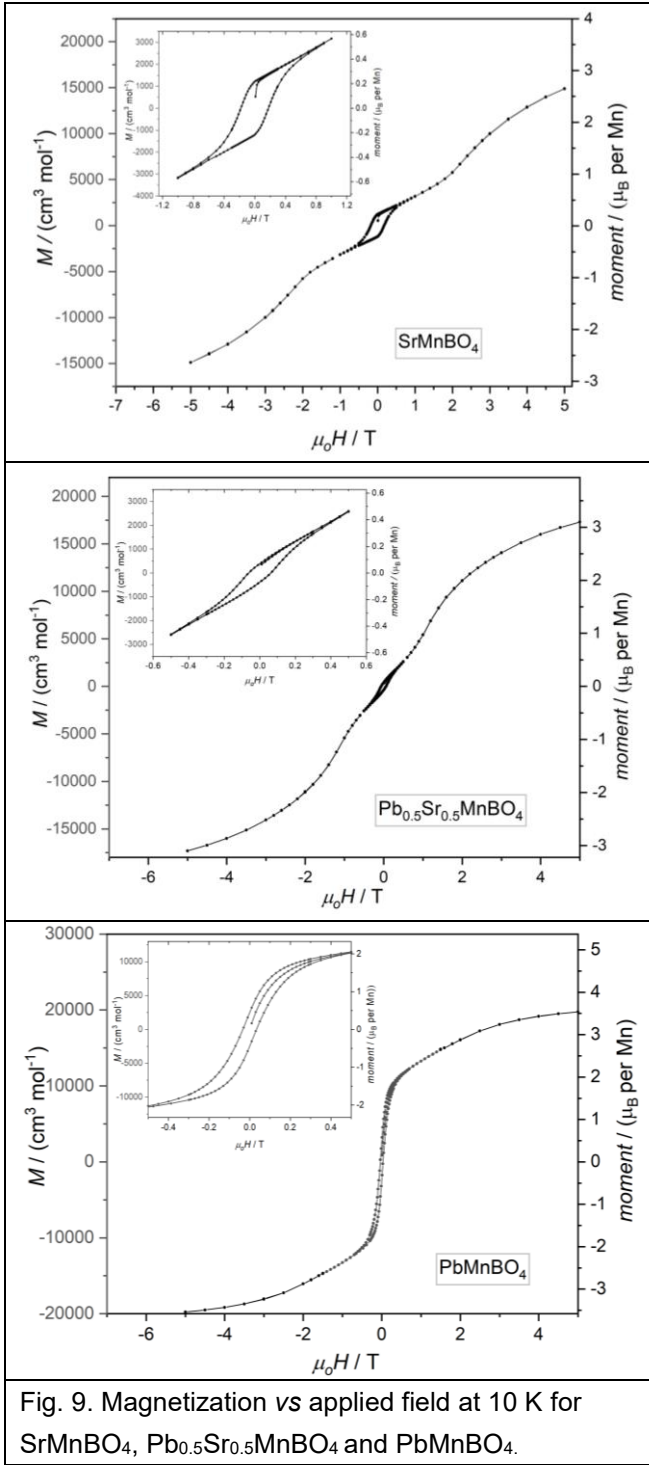
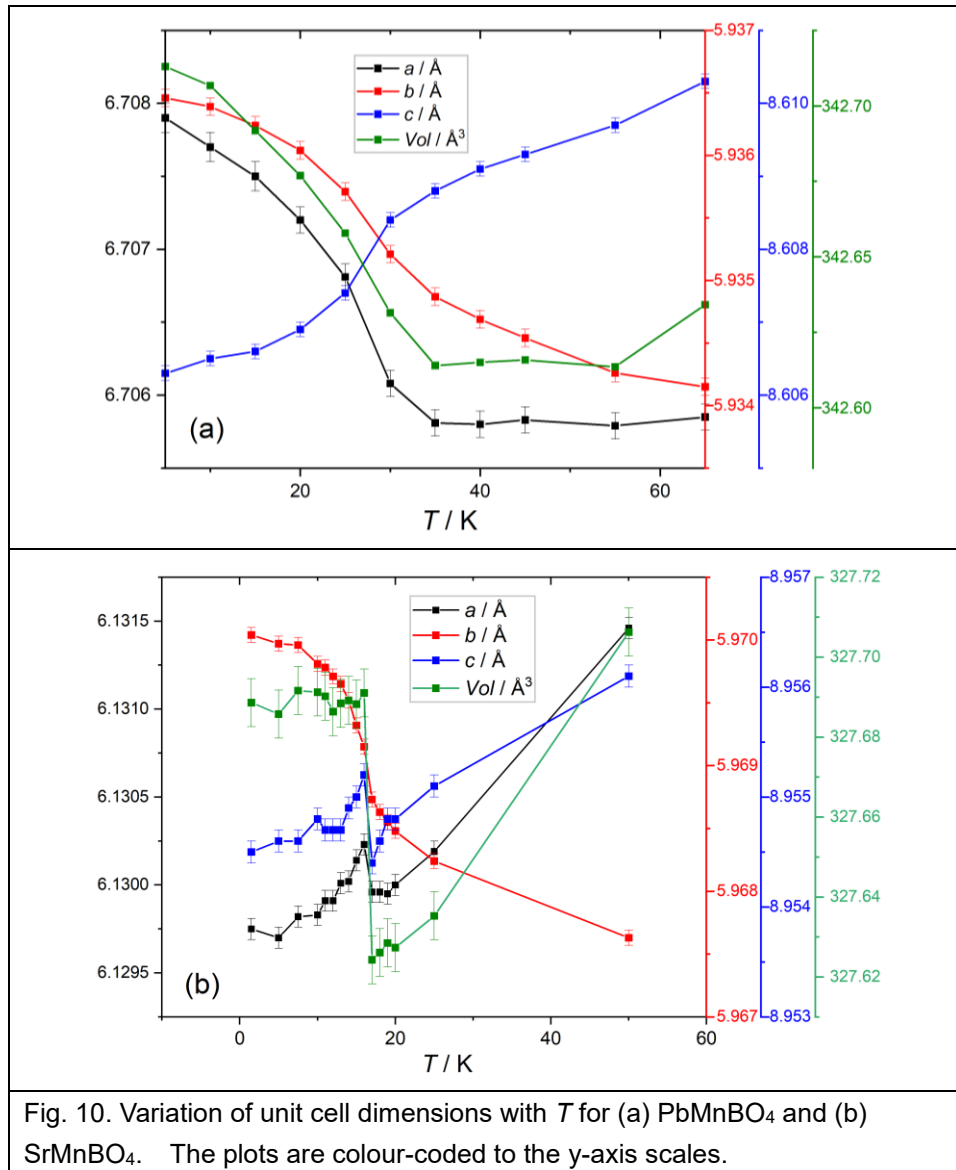


Fig. 9. Magnetization vs applied field at 10 K for SrMnBO₄, Pb_{0.5}Sr_{0.5}MnBO₄ and PbMnBO₄.

PbMnBO₄ shows more gradual changes especially for the *b*-axis. The expansion along [010] appears similar in both phases and the strain is probably dominated by the common FM chains of MnO₆ octahedra in this direction. Significantly, the results suggest that structural strain is occurring in the direction of the chains at temperatures significantly above that for 3D order; this is marked for

exchange). Defining the magnetostriction constant for *a* as $\lambda_{100} = (a_{1.5K} - a') / a'$ (where *a'* applies to just above the ordering temperature) *etc.*, then for PbMnBO₄: $\lambda_{100} = 3.0 \times 10^{-4}$, $\lambda_{010} = 3.0 \times 10^{-4}$, $\lambda_{001} = -3.0 \times 10^{-4}$, $\lambda_{vol} = 3.0 \times 10^{-4}$; for SrMnBO₄ $\lambda_{100} = 0.4 \times 10^{-4}$, $\lambda_{010} = 0.7 \times 10^{-4}$, $\lambda_{001} = 0.8 \times 10^{-4}$, $\lambda_{vol} = 2.0 \times 10^{-4}$. The structural changes reflect the effects of structural strains associated with ordering of the magnetic moments and significant magnetostriction is usually linked with magnetocrystalline anisotropy which here will be provided by the large Mn³⁺ Jahn-Teller distortion.^{33,34} All constants indicate expansion on cooling through *T_c* / *T_N* except for λ_{001} for PbMnBO₄. Unfortunately, it is difficult to analyse the details of the magnetostriction because no significant change to structural parameters are suggested by the NPD refinements except for the changes in unit cell size. The opposing signs of λ_{001} for PbMnBO₄ and SrMnBO₄ probably relate to the switch between FM and AFM inter-chain order. We also see that the changes in dimensions for SrMnBO₄ are very sharp except for *b*, whereas

PbMnBO₄ and is supportive of short-range FM order within the chains for $T > T_c$. It is also interesting to note that the spontaneous increase in a and decrease in c that occur in PbMnBO₄ on cooling through T_c continues the trend seen when Pb is substituted for Sr in AFM SrMnBO₄ ($a = 6.14892(3) \text{ \AA}$; $c = 8.97067(6) \text{ \AA}$) to form PbMnBO₄ ($a = 6.69380(5) \text{ \AA}$; $c = 8.63691(7) \text{ \AA}$) with dominant FM inter-chain magnetic exchange. It is therefore likely that the magnetostriction provides additional stabilization of the inter-chain FM ground state in PbMnBO₄.



The magnetostriction behavior of PbMnBO₄ and SrMnBO₄ reflects the similarities and differences between the magnetic exchange interactions in these structurally related materials. Both phases display intra-chain FM behavior in accordance with the predictions based on the

Goodenough-Kanamori-Anderson (GKA) rules^{35–37} for $\sim 90^\circ$ M–O–M (M = transition metal) links and the detailed information in Table 4. For a d^4 high-spin cation (e.g. Mn^{3+}), an M–O–M link will provide AFM exchange when the O is bonded to empty (d^0) and half-full (d^1) orbitals and FM for $d^0 \dots d^0$ and $d^1 \dots d^1$. For all samples under current investigations, Table 4 shows that the long Mn–O3–Mn bonds involve the singly-occupied Mn d_{z^2} orbitals and the shorter Mn–O1–Mn bonds are formed by the empty $d_{x^2-y^2}$ orbital; hence all bonds linking Mn in the chains give FM exchange between neighbouring Mn ions. Although the mechanism relies on relatively weak electron exchange interactions to maximize the unpaired electron spin on the orthogonal $2p$ orbitals on O1 and O3, this will be the primary basis for the intra-chain FM behavior. But what causes the change from FM inter-chain exchange in PbMnBO_4 to AFM exchange in SrMnBO_4 ? In Figs. 11 and 12 we explore the relevant structural differences and their possible magnetic consequences.

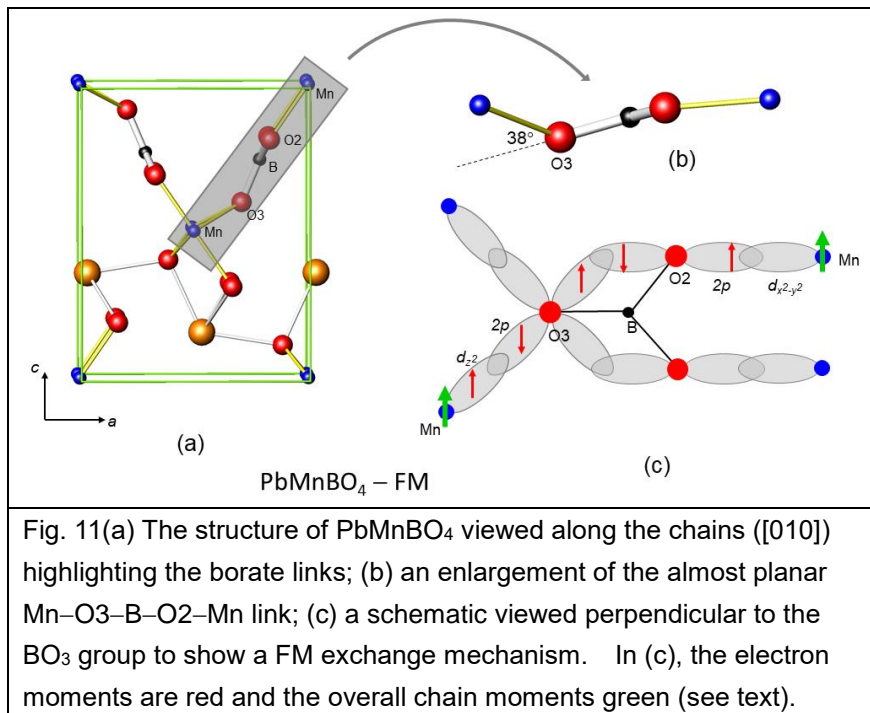
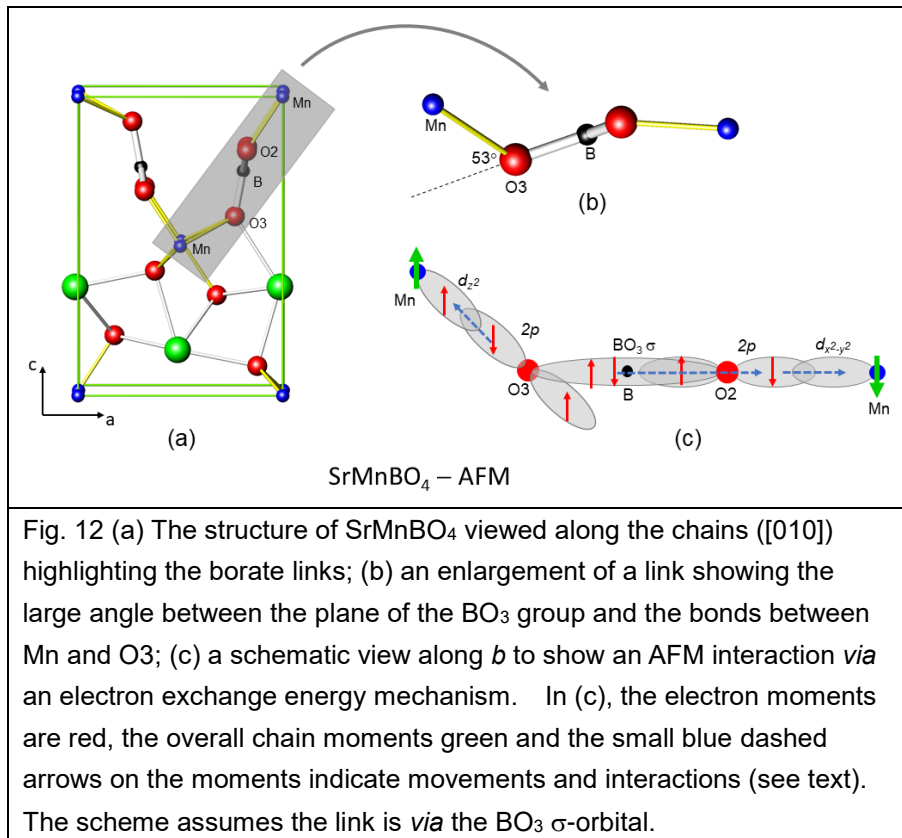


Fig. 11(a) shows the structure of PbMnBO_4 highlighting the most obvious magnetic pathway between the closest FM chains; this involves the borate group and the link is enlarged in Fig. 11(b). The linkage is quite flat (Fig. 11(b)) although the figure shows that the Mn ions bonded to O3 are out-of-plane. If we assume that the O $2p$ -orbitals are

directed towards the Mn ions, as is normal for 90° exchange (*vide supra*) then they cannot contribute significantly to the BO_3 σ -orbital as illustrated in Fig. 11(c), which shows the relevant orbitals viewed perpendicular to the plane of the borate group. The BO_3 σ -orbital may primarily be derived from the O $2s$ orbitals, but this is not important for the current discussion. The GKA rules^{35–37} may be applied to several combinations of atomic/molecular orbitals to provide FM superexchange (SE) interaction

between the Mn ions *via* the BO_3 groups. However, Fig. 11(c) highlights that a super-superexchange (SSE) mechanism should also be considered and would comprise the $\text{Mn}\cdots\text{O3}\cdots\text{O2}\cdots\text{Mn}$ interaction where O3 and O2 form an edge of the borate group.



This mechanism can be stronger than simple SE and is favoured by large Mn-O3-O2 and Mn-O2-O3 angles and a short O-O distance.^{38,39} The covalent bonding in BO_3 results in a very short O-O distance (2.38 \AA) which is ideal for orbital overlap. The Mn-O-O angles for PbMnBO_4 are 148° and 155° which should also provide suitable orbital overlap. We

therefore favour this fairly simple SSE exchange mechanism for PbMnBO_4 ; it is illustrated in Fig. 11(c) for one link between the occupied d_{z^2} orbital of a Mn ion in one chain and the empty $d_{x^2-y^2}$ orbital of a Mn in an adjacent chain.

In SrMnBO_4 , we seek a different mechanism that can rationalize the AFM inter-chain exchange – the Mn ions bonded to O3 are now moved further away from the plane containing the BO_3 group as seen in Figs. 12(a) and (b). The angle shown as 38° for PbMnBO_4 (Fig. 11 (b)) is now 53° for SrMnBO_4 and the Mn-O-O angles that are 148° and 155° for PbMnBO_4 are reduced to 136° and 149° . The $2p$ orbitals on O3 are now unsuitable for involvement in the BO_3 σ -orbital or any π -bonding in the borate group. The FM SSE pathway now appears too weak, which is supported by the fact that the angle of 38° for PbMnBO_4 (Fig. 11 (b)) is 53° , 53° and 47° for the three phases with AFM inter-chain interactions, SrMnBO_4 , gaufreyite and $\text{Pb}_{0.5}\text{Sr}_{0.5}\text{MnBO}_4$, respectively. We

propose a mechanism based on electron exchange energy considerations for these phases and illustrated in Fig. 12(c). This mechanism, the basis of Hund's rules, relies on second-order perturbation theory; it is therefore usually quite weak but provides the FM coupling in the 90° Mn–O–Mn intra-chain interactions. In simple terms (and represented in Fig. 12(c)), the excess spin-up density on O3 resulting from partial transfer of a spin-down electron to the Mn d_{z^2} orbital allows stabilization when there exists spin-up for unpaired electrons in the BO₃ σ -orbital and also in the 2p orbital on O2. This is achieved by transfer of spin-down electron to the Mn $d_{x^2-y^2}$ orbital and gives overall AFM interaction. The weakness of this exchange explains why T_N for SrMnBO₄ and Pb_{0.5}Sr_{0.5}MnBO₄ is ~ 16 K compared with T_c ~ 30 K for PbMnBO₄ with FM inter-chain links.

Only subtle structural effects differentiate between the proposed inter-chain exchange mechanisms for FM PbMnBO₄ and AFM SrMnBO₄. These mechanisms are specific to the observed orbital order in the Jahn-Teller stabilised Mn³⁺ ions, and it is relevant to note that PbCrMnO₄ and PbFeBO₄ show FM inter-chain interactions. In fact, for the Cr³⁺ and Fe³⁺ electron configurations, the mechanism outlined for SrMnBO₄ would account for FM order between the chains in these compounds.

Neutron powder diffraction with applied field

In order to examine the effects of magnetic field on magnetic structure, NPD data were collected at various fields and temperatures for PbMnBO₄ and SrMnBO₄ samples. An unavoidable problem for polycrystalline samples is that crystallites will experience fields in different directions. To ensure a random distribution of crystal orientations, sintered pellets were used with crystals spatially locked even in magnetic fields. Unless there is a highly dominant easy magnetization axis, for orthorhombic structures with orthogonal axes, an applied magnetic field averaged over all crystals should introduce magnetic moments with equal components along the three Cartesian axes consistent with the magnetic unit cell, *i.e.* $m_x = m_y = m_z$. This was checked by comparing the field-induced magnetic neutron scattering in paramagnetic PbMnBO₄ with simulated magnetic diffraction profiles. For PbMnBO₄ at 35 K (in the paramagnetic region), the difference between the diffraction profiles in 4 T and 0 T is shown in Fig. 13(a). Simulations of profiles for moments in

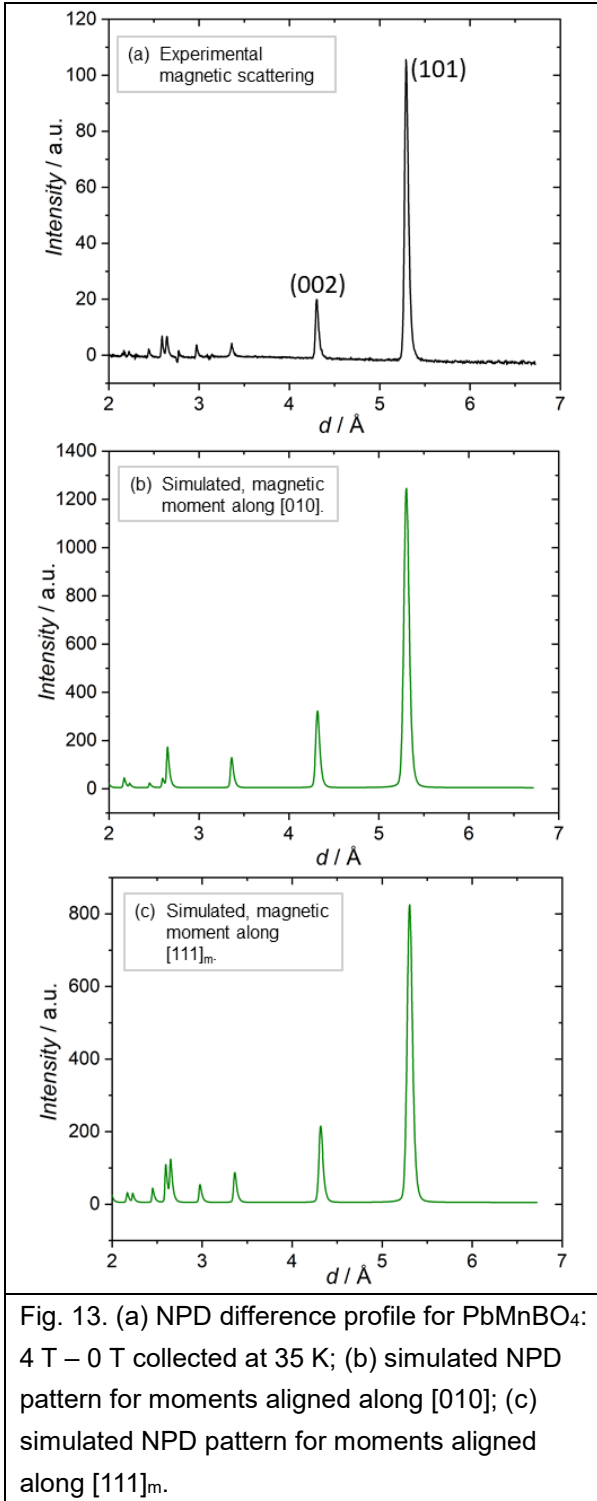


Fig. 13. (a) NPD difference profile for PbMnBO_4 : 4 T – 0 T collected at 35 K; (b) simulated NPD pattern for moments aligned along [010]; (c) simulated NPD pattern for moments aligned along $[111]_m$.

various orientations revealed only two that could possibly be consistent with the observed scattering – those with moments along [010] (Fig. 13(b)) or along $[111]_m$ (Fig. 13(c)). The subscript 'm' (as in $[111]_m$) will be used to indicate a magnetic moment vector $[xyz]_m$ referred to Cartesian axes; the direction does not coincide with the structural vector $[xyz]$ and, although $[100] \equiv [100]_m$, $[111]_m$ is **not** perpendicular to the (111) planes. It is seen that both models provide major scattering in the (101) and (002) reflections at $d \sim 5.3 \text{ \AA}$ and $d \sim 4.3 \text{ \AA}$, respectively. The difference between the two possibilities is observed at shorter d -spacings: at $\sim 2.6 \text{ \AA}$ and $\sim 3.0 \text{ \AA}$ the experimental scattering is reproduced only with moments along $[111]_m$. Obtaining the profile shown in Fig. 13(a) proved important since these critical low intensity peaks are masked by nuclear scattering in Rietveld refinements. Rietveld refinement residuals, however, fully supported constraining the moments to the $[111]_m$ direction. The Rietveld refinement plots at 35 K in 4 T are shown in Fig. S3. The $[111]_m$ direction for the induced moment was found to be true for SrMnBO_4 also, and all subsequent analysis of data obtained in applied fields was consistent with this orientation. The effects of

magnetic fields both below and above T_d/T_N were examined for PbMnBO_4 and SrMnBO_4 .

The effects of an applied magnetic field on the direction and magnitude of the principal FM moment in PbMnBO_4 at 1.5 K are shown in Fig. 14. It is seen that the moment gradually rotates

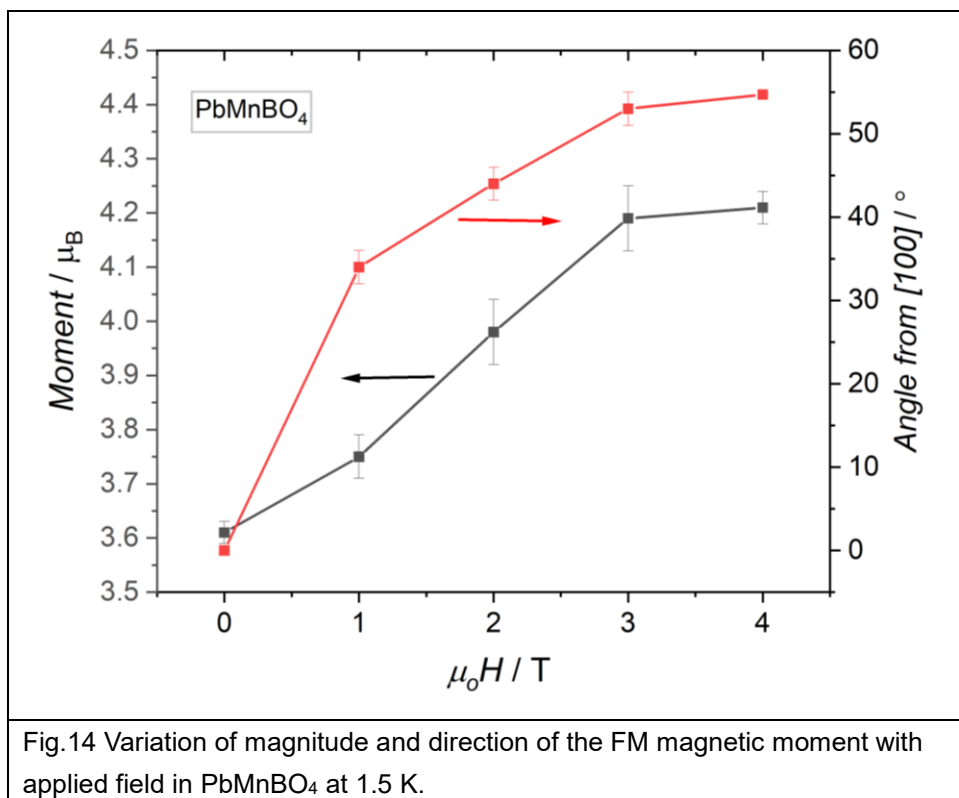


Fig. 14 Variation of magnitude and direction of the FM magnetic moment with applied field in PbMnBO₄ at 1.5 K.

from being aligned along the *a*-axis to a direction with equal components along all three axes. This direction makes an angle of 54.7° with *a*, and we see that saturation occurs at ~3 T with a moment of 4.0 μ_B , in agreement with that expected for Mn³⁺ with no orbital contribution to the moment. For

SrMnBO₄,

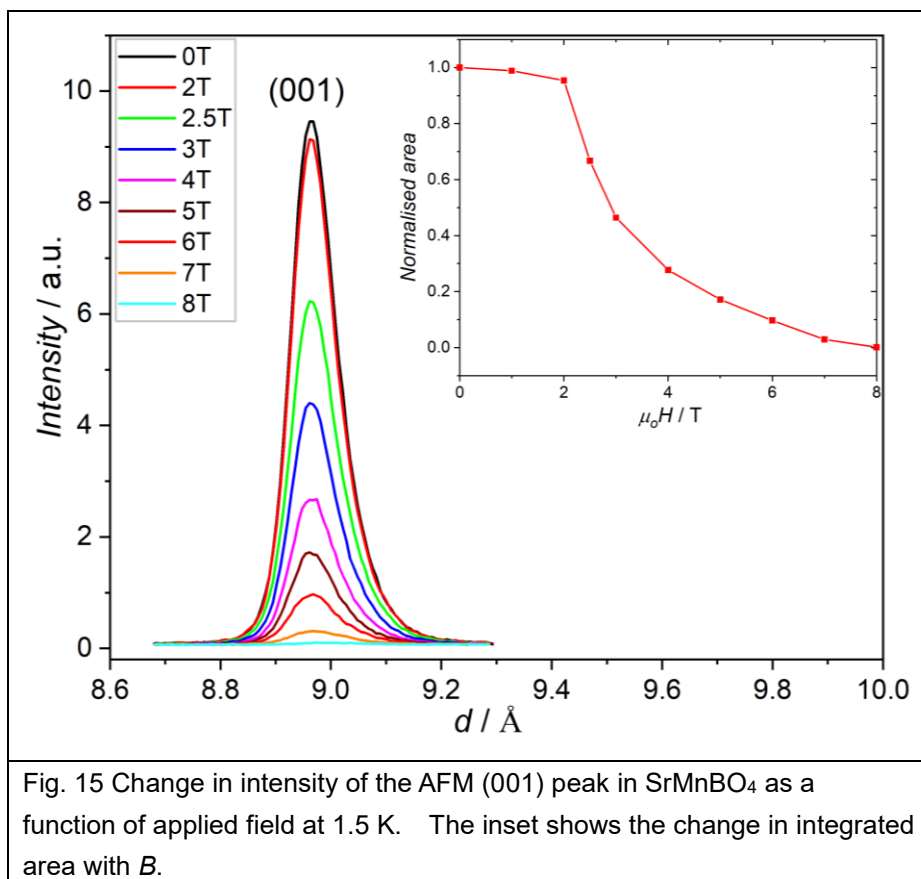


Fig. 15 Change in intensity of the AFM (001) peak in SrMnBO₄ as a function of applied field at 1.5 K. The inset shows the change in integrated area with *B*.

with opposed moments along *a*, it is not straightforward to monitor exactly the change in moment as a function of applied field. However, the very large, totally magnetic (001) diffraction peak gives us a precise measure of the change in the AFM component with applied field. Data for 1.5 K are presented in Fig. 15, which shows that the AFM order is

not disrupted at fields up to ~ 2 T and the diffraction peak then decreases quite smoothly with field; however, the AFM order disappears completely only at 8 T. The build-up of FM order was explored using Rietveld refinements by assuming that the applied field introduces a FM moment, which can be resolved equally along the three axes (along $[111]_m$). This can then be modelled by using two magnetic phases: one AFM which will decrease with field and a FM phase with equal components m_x , m_y and m_z that increases with field. In the refinements, because of the correlation between magnetic moment and phase fraction, the phase fractions of the two components were fixed at 1.0, but the moments were varied and allowed calculation of the separate moments for each phase and hence the total ordered moment as shown in Fig. 16. This figure also includes data for the AFM moment

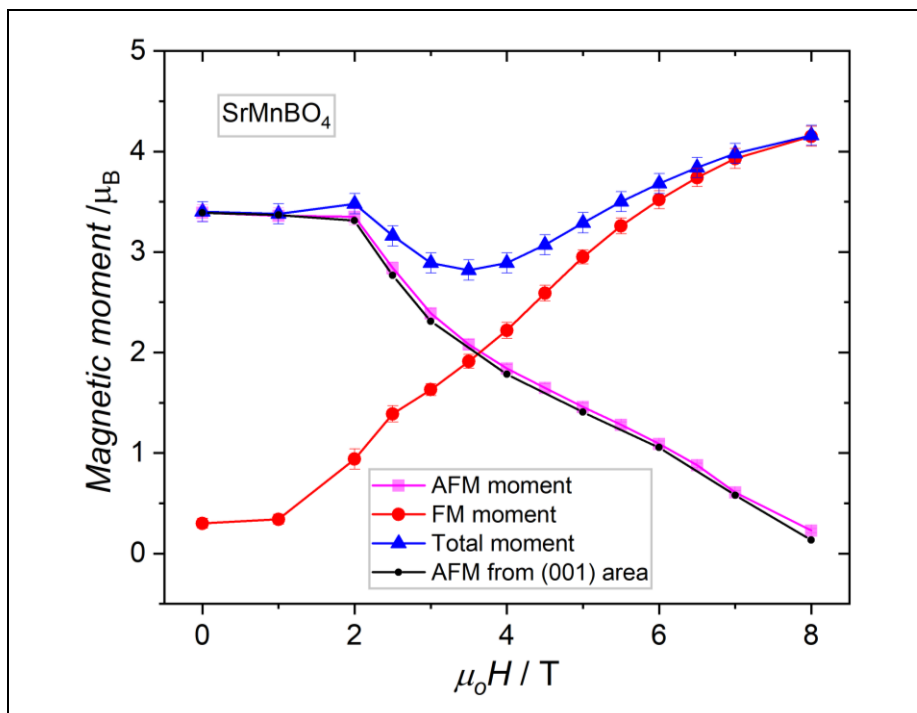


Fig. 16 AFM (along $[100]$) and FM (along $[111]$) contributions to the overall ordered moment in SrMnBO_4 as a function of applied field at 1.5 K from Rietveld refinements. The AFM moment is compared with that from normalising the (001) peak area of Fig. 15.

calculated from the (001) peak areas shown in Fig. 15. Since the peak area is proportional to m^2 , the normalized moment (m_o) was obtained from $m_o = 3.39 \times \sqrt{A/A_o}$ where A is the peak area and A_o the area at 1.5 K. The complete agreement between the two estimates of the AFM moment give confidence that the data in Fig. 16 are a good

representation of the magnetic changes occurring. It is seen that applied fields of $\mu_0 H \leq 2$ T fail to overcome the AFM exchange energy but at higher fields, the FM component increases until saturation occurs – but only at 8 T. At this field the FM moment is in the $[111]_m$ direction because of powder averaging, as was seen for PbMnBO_4 . SrMnBO_4 is therefore significantly less sensitive to

applied field than PbMnBO_4 where saturation is achieved at 3 T. The saturated moment in SrMnBO_4 is determined as $4.1(1) \mu_B$. The model used suggests that for fields in the range 2–5 T, the total ordered magnetic moment is smaller than expected (Fig. 16) and is indicative of some magnetic disorder in these intermediate fields because of the opposing interactions of the AFM exchange energy and the applied field direction. Representative NPD Rietveld refinement plots at intermediate applied magnetic fields are shown in Fig. S4 (PbMnBO_4 at 2 T) and S5 (SrMnBO_4 at 4.5 T). It is important to note that the behavior of SrMnBO_4 (AFM inter-chain exchange) is very different from that of gaufreyite (frustrated AFM with 120° between the ordered moments), which at 100 mK becomes 90% FM in a field of 1 T and saturates at 3 T.¹⁷ Although this may predict inferior MCE behavior for SrMnBO_4 , the behavior near and above T_N is more important; variable field NPD data were therefore collected for PbMnBO_4 and SrMnBO_4 in the paramagnetic region.

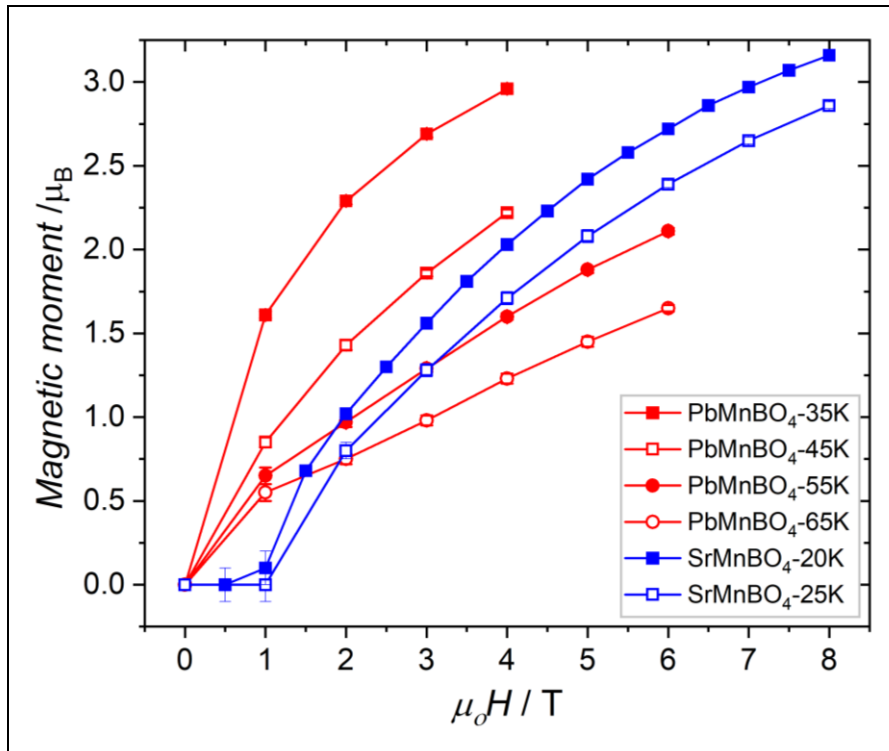
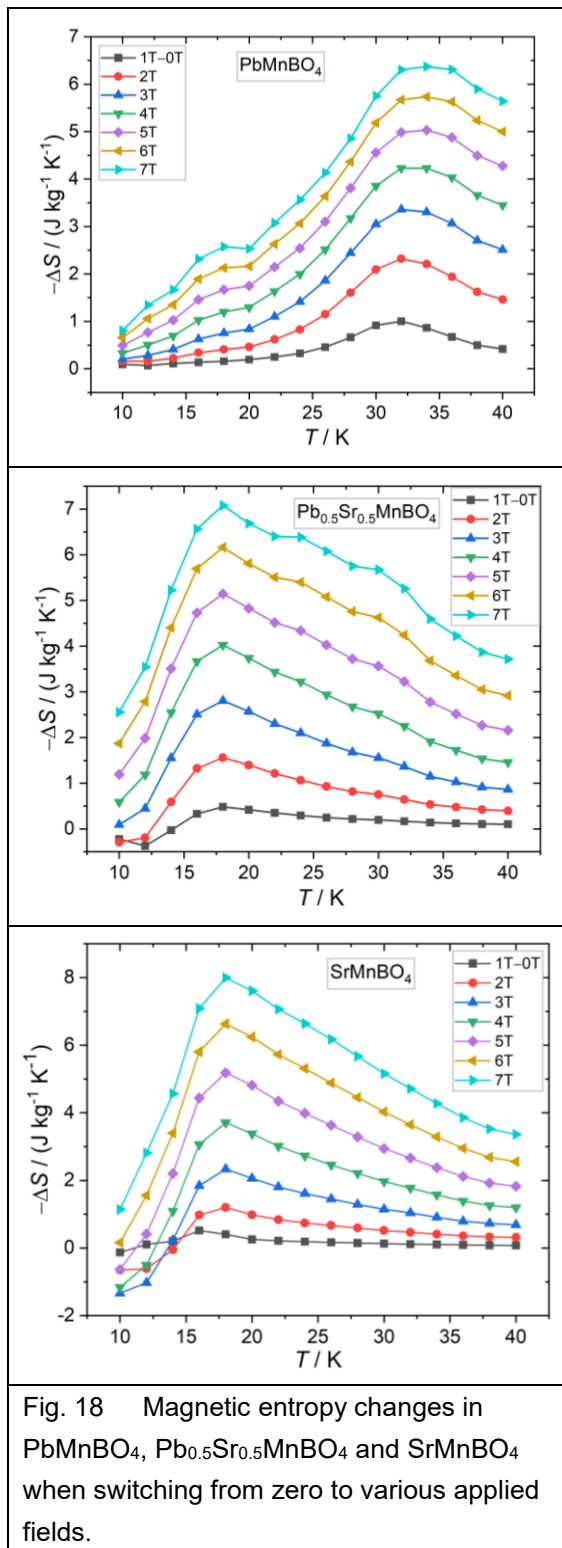


Fig. 17 Variation of the FM magnetic moment induced by applied fields above the ordering temperatures of PbMnBO_4 and SrMnBO_4 .

Fig. 17 shows the variation of the total FM moment with applied magnetic field for PbMnBO_4 and SrMnBO_4 at temperatures above T_c and T_N , respectively. It is seen that at respective temperatures of 35 K and 20 K (~ 5 K above the ordering temperatures), the moment of PbMnBO_4 is 57% saturated at 2 T and 74% at 4 T; at the same fields, SrMnBO_4 is only 26% and 51% saturated.

In comparison, gaufreyite at 15 K (again ~ 5 K above T_N) is 75% saturated at 3 T.¹⁷ This suggests that PbMnBO_4 could display very good MCE behavior at temperatures of ~ 30 K and above, but SrMnBO_4 would be expected to be less exciting. However, the lower magnetic ordering

temperature for SrMnBO₄ may prove useful at the boiling point of hydrogen. The MCE properties of all three samples were therefore measured indirectly using magnetization data.



Magnetocaloric properties

The magnetic entropy changes for applied fields up to 7 T were determined for all three samples as described in the Experimental section and the results shown in Fig. 18 refer conventionally to 1 kg of sample. All samples give a maximum in entropy change at a temperature slightly above that of the ordering temperature. In high fields, all three samples show similar values for the maximum $-\Delta S$, e.g. $\sim 6 \text{ J kg}^{-1} \text{ K}^{-1}$ at 6 T. At lower fields, PbMnBO₄ shows less reduction than the other samples probably because the field does not have to overcome an AFM exchange energy. We also see that above T_N / T_C , $-\Delta S$ decreases relatively slowly which

is consistent with there being a significant field response in agreement with the presence of short-range FM order within the chains of MnO₆ octahedra in all compounds. The entropy changes are excellent for this temperature range where very few materials exhibit high MCE characteristics. The best proven material for operation at 20 K, needed for hydrogen liquefaction, is gaufreyite¹⁷ and Fig. 19(a) gives comparative data for this material and those described here at a low field (2 T) and a high field (6 T). It is clear that gaufreyite

has superior properties at low temperatures, including 20 K. However, data for this mineral were

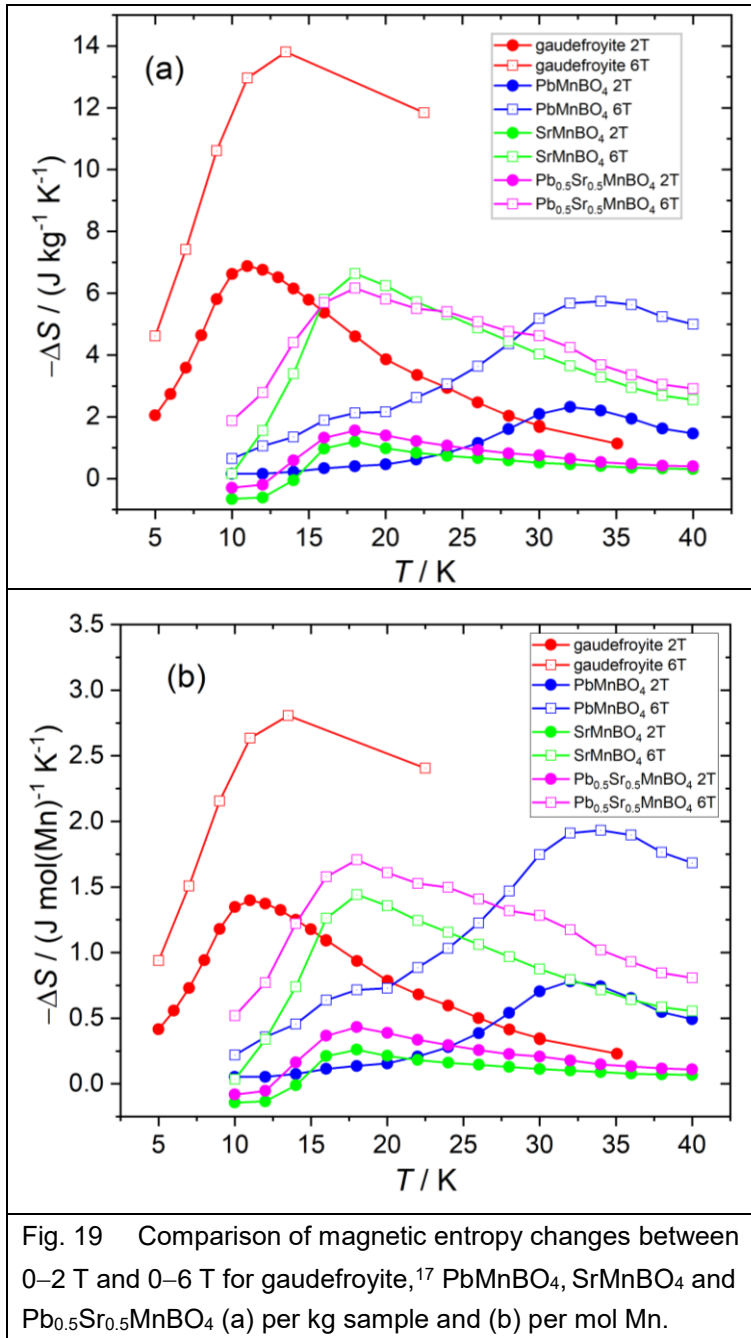


Fig. 19 Comparison of magnetic entropy changes between 0–2 T and 0–6 T for gaufreyite,¹⁷ PbMnBO_4 , SrMnBO_4 and $\text{Pb}_{0.5}\text{Sr}_{0.5}\text{MnBO}_4$ (a) per kg sample and (b) per mol Mn.

collected from a single crystal with easy-axis orientation, and powder-averaging to allow more direct comparison would decrease the $-\Delta S$ values by $\sim 20\%$.

For $T > \sim 25$ K, it appears that even at 2 T, PbMnBO_4 performs better than gaufreyite. More realistic comparisons can be made using data normalized on the $-\Delta S$ per mol Mn rather than per kg, and these are shown in Fig. 19.

We see that the mass of Pb plays an important role in determining the MCE performance and, allowing for the fact that PbMnBO_4 is in polycrystalline form, $-\Delta S_{\text{max}}$ for both 2 T and 6 T appear very similar for PbMnBO_4 and gaufreyite. SrMnBO_4 and $\text{Pb}_{0.5}\text{Sr}_{0.5}\text{MnBO}_4$ are inferior at 2 T but good at 6 T. In fact, at high field the solid solution $\text{Pb}_{1-x}\text{Sr}_x\text{MnBO}_4$ has very good MCE behavior over the extended temperature range $15 \text{ K} < T < 40 \text{ K}$. The comparable behavior

of gaufreyite and PbMnBO_4 near their Curie temperatures suggests that the magnetic frustration perpendicular to the MnO_6 chains in gaufreyite is not essential for the provision of excellent MC properties, but a large difference between the intra-chain and inter-chain magnetic exchange energies is needed. In fact, since we ideally need a magnetic ordering temperature of ~ 20 K for hydrogen liquefaction applications, this will be too high for highly frustrated materials.

Conclusions

The structures, both nuclear and magnetic, of PbMnBO_4 , SrMnBO_4 and $\text{Pb}_{0.5}\text{Sr}_{0.5}\text{MnBO}_4$ have been determined to explore their applicability for MC cooling at temperatures suitable for hydrogen liquefaction, 20 K. PbMnBO_4 is FM with a small AFM contribution whereas SrMnBO_4 and $\text{Pb}_{0.5}\text{Sr}_{0.5}\text{MnBO}_4$ display canted AFM magnetic order with lower magnetic ordering temperatures. All materials have strong FM coupling within the chains of MnO_6 octahedra and this relates primarily to the 90° Mn–O–Mn exchange interactions. The difference in inter-chain coupling is attributed to differences in the links which involve the BO_3 groups and rationalization of the switch from FM to AFM is possible. Exchange magnetostriction is observable for PbMnBO_4 and SrMnBO_4 and to some extent can be related to the different exchange interactions in these compounds. The broad magnetostriction along [010], the chain direction, is consistent with short-range FM order existing within the chains above the magnetic ordering temperatures. The change of magnetic properties when subjected to applied magnetic fields was focused on the ability of these materials to exhibit useful MCE behavior at temperatures of ~ 20 K, necessary for liquefaction of hydrogen but higher than can be achieved for existing well-characterized materials. The magnetic properties showed that for SrMnBO_4 and $\text{Pb}_{0.5}\text{Sr}_{0.5}\text{MnBO}_4$, low fields had little effect on the magnetic properties because, presumably, of the inhibition caused by the energy to disrupt the inter-chain AFM order. In contrast, PbMnBO_4 seemed more sensitive to fields both below and above T_c . This was confirmed in calculations of $-\Delta S$, the change in magnetic entropy on removal of an applied field. In particular, PbMnBO_4 has excellent MCE behavior between 25 K and 40 K, similar to that reported for alloys,⁸ but unfortunately too high for liquefying hydrogen; nevertheless, PbMnBO_4 and related materials could be of interest for a higher temperature cooling stage since at present no single material can cover the cooling from room temperature to 20 K. It is also possible to extract pointers towards improved materials for operation at lower temperatures. The frustrated AFM interactions between the chains in the mineral gaufroyite appear important for its excellent low-field behavior, although PbMnBO_4 appears very good in this respect at its transition temperature of 30 K. The problem with PbMnBO_4 can be traced to two sources: its relatively heavy molecular mass and its high Curie

temperature, certainly for operation at 20 K. It seems clear, however, that the strong intra-chain FM interactions both below and above T_c are vital for the properties of the materials studied. We anticipate that the substitution of Pb for a lighter element and weakening slightly the inter-chain magnetic exchange (for a lower T_c) should provide the very best MCE behavior for development as a material for hydrogen liquefaction *via* energy-efficient adiabatic MC cooling. In addition, we note a molecular field analysis that for quasi-one-dimensional FM chains with weak inter-chain interactions, the 3-dimensional magnetic ordering temperature will vary not only with the inter-chain exchange energy but will also be proportional to the intra-chain correlation length.⁴⁰ Reduction of the intra-chain FM Mn–Mn interactions could be achieved by introducing low concentrations of M^{3+} cations into the chains. These could be either non-magnetic (*e.g.* Sc^{3+}) or magnetic with configurations that disrupt the 90° FM Mn–O–Mn interactions (*e.g.* Cr^{3+} or Fe^{3+}). In this way, significantly enhanced MC behavior might be achieved at temperatures close to 20 K.

Associated Content

The Supporting Information is available free of charge at:

NPD Rietveld refinement plots for: $PbMnBO_4$ at 300 K; $Pb_{0.5}Sr_{0.5}MnBO_4$ at 300 K; $PbMnBO_4$ at 35 K in 4 T; $PbMnBO_4$ at 1.5 K in 2 T; $SrMnBO_4$ at 1.5 K in 4.5 T.

Acknowledgements

The present work was supported by the National Natural Science Foundation of China (No. 51772304), EPSRC (2285028) and the University of Birmingham (Birmingham Fellowship). The authors acknowledge the Science and Technology Facility Council (STFC) for the provision of neutron beam facilities. Neutron diffraction data analysed in this report can be obtained at <https://doi.org/10.5286/ISIS.E.RB1920247>.

References

- (1) Qu, Y. H.; Cong, D. Y.; Li, S. H.; Gui, W. Y.; Nie, Z. H.; Zhang, M. H.; Ren, Y.; Wang, Y. D. Simultaneously Achieved Large Reversible Elastocaloric and Magnetocaloric Effects and Their Coupling in a Magnetic Shape Memory Alloy. *Acta Mater.* **2018**, *151*, 41–55. <https://doi.org/10.1016/j.actamat.2018.03.031>.
- (2) Yu, B.; Liu, M.; Egolf, P. W.; Kitanovski, A. A Review of Magnetic Refrigerator and Heat Pump Prototypes Built before the Year 2010. *Int. J. Refrig.* **2010**, *33* (6), 1029–1060. <https://doi.org/10.1016/j.ijrefrig.2010.04.002>.
- (3) Liu, J.; Gottschall, T.; Skokov, K. P.; Moore, J. D.; Gutfleisch, O. Giant Magnetocaloric Effect Driven by Structural Transitions. *Nat. Mater.* **2012**, *11* (7), 620–626. <https://doi.org/10.1038/nmat3334>.
- (4) Zhang, H.; Shen, B. G.; Xu, Z. Y.; Shen, J.; Hu, F. X.; Sun, J. R.; Long, Y. Large Reversible Magnetocaloric Effects in ErFeSi Compound under Low Magnetic Field Change around Liquid Hydrogen Temperature. *Appl. Phys. Lett.* **2013**, *102* (9), 092401. <https://doi.org/10.1063/1.4794415>.
- (5) Shinde, K. P.; Jang, S. H.; Ranot, M.; Sinha, B. B.; Kim, J. W.; Chung, K. C. Large Magnetic Entropy Change at Cryogenic Temperature in Rare Earth HoN Nanoparticles. *RSC Adv.* **2016**, *6* (79), 75562–75569. <https://doi.org/10.1039/C6RA16356D>.
- (6) Li, R. Enhancing the Magnetocaloric Effect of a Paramagnet to above Liquid Hydrogen Temperature. *Energy Technol.* **2019**, *7* (5), 1801070. <https://doi.org/10.1002/ente.201801070>.
- (7) Numazawa, T.; Kamiya, K.; Utaki, T.; Matsumoto, K. Magnetic Refrigerator for Hydrogen Liquefaction. *Cryogenics (Guildf)*. **2014**, *62*, 185–192. <https://doi.org/10.1016/j.cryogenics.2014.03.016>.
- (8) Campoy, J. C. P.; Plaza, E. J. R.; Coelho, A. A.; Gama, S. Magnetoresistivity as a Probe to the Field-Induced Change of Magnetic Entropy in RAI_2 Compounds (R=Pr, Nd, Tb, Dy, Ho, Er). *Phys. Rev. B* **2006**, *74* (13), 134410. <https://doi.org/10.1103/PhysRevB.74.134410>.

- (9) Zhitomirsky, M. E. Enhanced Magnetocaloric Effect in Frustrated Magnets. *Phys. Rev. B* **2003**, 67 (10), 104421. <https://doi.org/10.1103/PhysRevB.67.104421>.
- (10) Schnack, J.; Schmidt, R.; Richter, J. Enhanced Magnetocaloric Effect in Frustrated Magnetic Molecules with Icosahedral Symmetry. *Phys. Rev. B* **2007**, 76 (5), 054413. <https://doi.org/10.1103/PhysRevB.76.054413>.
- (11) Sosin, S. S.; Prozorova, L. A.; Smirnov, A. I.; Golov, A. I.; Berkutov, I. B.; Petrenko, O. A.; Balakrishnan, G.; Zhitomirsky, M. E. Magnetocaloric Effect in Pyrochlore Antiferromagnet $Gd_2Ti_2O_7$. *Phys. Rev. B* **2005**, 71 (9), 094413. <https://doi.org/10.1103/PhysRevB.71.094413>.
- (12) Dixey, R. J. C.; Orlandi, F.; Manuel, P.; Mukherjee, P.; Dutton, S. E.; Saines, P. J. Emergent Magnetic Order and Correlated Disorder in Formate Metal-Organic Frameworks. *Philos. Trans. R. Soc. A Math. Phys. Eng. Sci.* **2019**, 377 (2149), 20190007. <https://doi.org/10.1098/rsta.2019.0007>.
- (13) Dixey, R. J. C.; Saines, P. J. Optimization of the Magnetocaloric Effect in Low Applied Magnetic Fields in $LnOHCO_3$ Frameworks. *Inorg. Chem.* **2018**, 57 (20), 12543–12551. <https://doi.org/10.1021/acs.inorgchem.8b01549>.
- (14) Dixey, R. J. C.; Stenning, G. B. G.; Manuel, P.; Orlandi, F.; Saines, P. J. Ferromagnetic Ising Chains in Frustrated $LnODCO_3$: The Influence of Magnetic Structure in Magnetocaloric Frameworks. *J. Mater. Chem. C* **2019**, 7 (42), 13111–13119. <https://doi.org/10.1039/C9TC04980K>.
- (15) Saines, P. J.; Paddison, J. A. M.; Thygesen, P. M. M.; Tucker, M. G. Searching beyond Gd for Magnetocaloric Frameworks: Magnetic Properties and Interactions of the $Ln(HCO_2)_3$ Series. *Mater. Horizons* **2015**, 2 (5), 528–535. <https://doi.org/10.1039/C5MH00113G>.
- (16) Hoffmann, C.; Armbruster, T.; Kunz, M. Structure Refinement of (001) Disordered Gaufreyite $Ca_4Mn^{3+}_3[(BO_3)_3(CO_3)O_3]$: Jahn-Teller-Distortion in Edge-Sharing Chains of $M^{3+}O_6$ Octahedra. *Eur. J. Mineral.* **1996**, 9 (1), 7–20. <https://doi.org/10.1127/ejm/9/1/0007>.
- (17) Li, R.; Li, G.; Greaves, C. Gaufreyite: A Mineral with Excellent Magnetocaloric Effect

- Suitable for Liquefying Hydrogen. *J. Mater. Chem. A* **2018**, *6* (13), 5260–5264.
<https://doi.org/10.1039/C7TA06883B>.
- (18) Li, R.; Manuel, P.; Orlandi, F.; Greaves, C. Magnetic Ordering of the Cryogenic Magnetic Cooling Mineral Gaudefroyite. *J. Mater. Chem. A* **2018**, *6* (42), 21149–21155.
<https://doi.org/10.1039/C8TA08851A>.
- (19) Park, H.; Lam, R.; Greedan, J. E.; Barbier, J. Synthesis, Crystal Structure, Crystal Chemistry, and Magnetic Properties of PbMBO₄ (M = Cr, Mn, Fe): A New Structure Type Exhibiting One-Dimensional Magnetism. *Chem. Mater.* **2003**, *15* (8), 1703–1712.
<https://doi.org/10.1021/cm0217452>.
- (20) Koo, H.-J.; Whangbo, M.-H. Density Functional Investigation of the Magnetic Properties of PbMBO₄ (M=Cr, Mn, Fe). *Solid State Commun.* **2009**, *149* (15–16), 602–604.
<https://doi.org/10.1016/j.ssc.2009.01.030>.
- (21) Xiang, H.; Tang, Y.; Zhang, S.; He, Z. Intra-Chain Superexchange Couplings in Quasi-1D 3d Transition-Metal Magnetic Compounds. *J. Phys. Condens. Matter* **2016**, *28* (27), 276003.
<https://doi.org/10.1088/0953-8984/28/27/276003>.
- (22) Pankrats, A.; Kolkov, M.; Martynov, S.; Popkov, S.; Krasikov, A.; Balaev, A.; Gorev, M. Peculiarities of a Magnetic Transition in a Quasi-One-Dimensional Ferromagnet PbMnBO₄. *J. Magn. Magn. Mater.* **2019**, *471*, 416–422. <https://doi.org/10.1016/j.jmmm.2018.09.098>.
- (23) Pankrats, A.; Sablina, K.; Eremin, M.; Balaev, A.; Kolkov, M.; Tugarinov, V.; Bovina, A. Ferromagnetism and Strong Magnetic Anisotropy of the PbMnBO₄ Orthoborate Single Crystals. *J. Magn. Magn. Mater.* **2016**, *414*, 82–89.
<https://doi.org/10.1016/j.jmmm.2016.04.042>.
- (24) Chapon, L. C.; Manuel, P.; Radaelli, P. G.; Benson, C.; Perrott, L.; Ansell, S.; Rhodes, N. J.; Raspino, D.; Duxbury, D.; Spill, E.; Norris, J. Wish: The New Powder and Single Crystal Magnetic Diffractometer on the Second Target Station. *Neutron News* **2011**, *22* (2), 22–25.
<https://doi.org/10.1080/10448632.2011.569650>.

- (25) Toby, B. H.; Von Dreele, R. B. GSAS-II : The Genesis of a Modern Open-Source All Purpose Crystallography Software Package. *J. Appl. Crystallogr.* **2013**, *46* (2), 544–549.
<https://doi.org/10.1107/S0021889813003531>.
- (26) Pecharsky, V. K.; Gschneidner, K. A. Magnetocaloric Effect from Indirect Measurements: Magnetization and Heat Capacity. *J. Appl. Phys.* **1999**, *86* (1), 565–575.
<https://doi.org/10.1063/1.370767>.
- (27) Shannon, R. D. Revised Effective Ionic Radii in Halides and Chalcogenides. *Acta Crystallogr.* **1976**, *A32*, 751–767. <https://doi.org/10.1107/S0567739476001551>.
- (28) Brown, I. D.; Altermatt, D. Bond-Valence Parameters Obtained from a Systematic Analysis of the Inorganic Crystal Structure Database. *Acta Crystallogr. Sect. B Struct. Sci.* **1985**, *41* (4), 244–247. <https://doi.org/10.1107/S0108768185002063>.
- (29) Mentré, O.; Dhaussy, A. C.; Abraham, F.; Suard, E.; Steinfink, H. Crystal Structure of $\text{Pb}_2\text{V}_3\text{O}_9$: Rietveld Refinement and Electron Lone-Pair Localization. The Magnetic Susceptibility of Sr^{2+} - Substituted Phases. *Chem. Mater.* **1999**, *11* (9), 2408–2416.
<https://doi.org/10.1021/cm990073l>.
- (30) Miller, S.; Love WF. *Tables of Irreducible Representations of Space Groups and Co-Representations of Magnetic Space Groups*; Pruett: Boulder, 1967.
- (31) Taroni, A.; Bramwell, S. T.; Holdsworth, P. C. W. Universal Window for Two-Dimensional Critical Exponents. *J. Phys. Condens. Matter* **2008**, *20* (27), 275233.
<https://doi.org/10.1088/0953-8984/20/27/275233>.
- (32) Bramwell, S. T.; Holdsworth, P. C. W. Universality in Two-dimensional Magnetic Systems. *J. Appl. Phys.* **1993**, *73* (10), 6096–6098. <https://doi.org/10.1063/1.353481>.
- (33) Ghatak, S. K.; Chaudhuri, I. A Possible Mechanism for Large Magnetostriction in Manganite System. *J. Magn. Magn. Mater.* **2003**, *261* (3), 442–448. [https://doi.org/10.1016/S0304-8853\(02\)01495-6](https://doi.org/10.1016/S0304-8853(02)01495-6).
- (34) Dionne, G. F. Origin of the Magnetostriction Effects from Mn^{3+} , Co^{2+} , and Fe^{2+} Ions in

Ferrimagnetic Spinel and Garnets. *J. Appl. Phys.* **1979**, *50* (6), 4263–4272.

<https://doi.org/10.1063/1.326459>.

- (35) Goodenough, J. B. Theory of the Role of Covalence in the Perovskite-Type Manganites [La,M(II)]MnO₃. *Phys. Rev.* **1955**, *100* (2), 564–573. <https://doi.org/10.1103/PhysRev.100.564>.
- (36) Kanamori, J. Superexchange Interaction and Symmetry Properties of Electron Orbitals. *J. Phys. Chem. Solids* **1959**, *10* (2–3), 87–98. [https://doi.org/10.1016/0022-3697\(59\)90061-7](https://doi.org/10.1016/0022-3697(59)90061-7).
- (37) Anderson, P. W. New Approach to the Theory of Superexchange Interactions. *Phys. Rev.* **1959**, *115* (1), 2–13. <https://doi.org/10.1103/PhysRev.115.2>.
- (38) Whangbo, M. H.; Koo, H. J.; Dai, D.; Jung, D. Interpretation of the Magnetic Structures of Cu₂Te₂O₅X₂ (X = Cl, Br) and Ca_{3.1}Cu_{0.9}RuO₆ on the Basis of Electronic Structure Considerations: Cases for Strong Super-Superexchange Interactions Involving Cu²⁺ Ions. *Inorg. Chem.* **2003**, *42* (12), 3898–3906. <https://doi.org/10.1021/ic020551l>.
- (39) Koo, H. J.; Dai, D.; Whangbo, M. H. Importance of Supersuperexchange Interactions in Determining the Dimensionality of Magnetic Properties. Determination of Strongly Interacting Spin Exchange Paths in a A₂Cu(PO₄)₂ (A = Ba, Sr), ACuP₂O₇ (Ba, Ca, Sr, Pb), CaCuGe₂O₆ and Cu₂UO₂(PO₄)₂ on the basis of Qualitative Spin Dimer Analysis. *Inorg. Chem.* **2005**, *44* (12), 4359–4365. <https://doi.org/10.1021/ic050159j>.
- (40) de Jongh, L. J. Introduction to Low-Dimensional Magnetic Systems. In *Magnetic Properties of Layered Transition Metal Compounds*; de Jongh, L. J., Ed.; Kluwer Academic Publishers: Dordrecht, 1990, pp 1–51.

TOC graphic.

